1	Climate feedbacks derived from spatial gradients in recent climatology
2	P. Goodwin ¹ , R. G. Williams ² , P. Ceppi ³ , and B. B. Cael ^{4,5}
3	¹ School of Ocean and Earth Science, University of Southampton, SO14 3ZH, UK.
4 5	² Department of Earth, Ocean and Ecological Sciences, School of Environmental Sciences, University of Liverpool, Liverpool, L69 3GP UK.
6	³ Department of Physics, Imperial College London, London, SW7 2AZ, UK.
7 8	⁴ Ocean Biogeosciences, National Oceanography Centre, European Way, Southampton, SO14 3ZH, UK.
9	⁵ Department of the Geophysical Sciences, University of Chicago, IL, USA
10	Corresponding author: Philip Goodwin (p.a.goodwin@soton.ac.uk)
11	
12	
13	First submitted 19 th August 2024.
14	Submitted in revised form 9 th June 2025.
15	Accepted for publication in Journal of Geophysical Research: Atmospheres, 10 th June 2025.
16	
17	Key Points:
18 19	 Earth's radiation budget is related to surface and atmospheric properties in recent climatology using simplified empirical relations
20 21	 Spatial variations in outgoing radiation are dominated by their dependence on surface temperature
22	 Climate feedbacks are evaluated spatially by differentiating the simplified empirical

relations with respect to surface temperature

Abstract

 Climate feedbacks, including Planck, surface albedo, water vapor-lapse rate (WVLR) and cloud feedbacks, determine how much surface temperatures will eventually warm to balance anthropogenic radiative forcing. Climate feedbacks remain difficult to constrain directly from temporal variation in observed surface warming and radiation budgets due to the pattern effect and low signal-to-noise ratio, with only order 1°C historic rise in surface temperatures and high uncertainty in aerosol radiative forcing. This study presents a new method to analyze climate feedbacks from observations by empirically fitting simplified reduced-physics relations for outgoing radiation at the top of the atmosphere (TOA) to observed spatial variation in climate properties and radiation budgets. Spatial variations in TOA outgoing radiation are dominated by the dependence on surface temperature: around 91% of the spatial variation in clear sky albedo, and 77% of spatial variation in clear sky TOA outgoing longwave radiation, is functionally explained by variation in surface temperatures. These simplified and observationally constrained relations are then differentiated with respect to spatial contrasts in surface temperature to reveal the Planck, fixed-cloud albedo (λ_{albedo}) and WVLR (λ_{WVLR}) climate feedbacks spatially for both clear sky and all sky conditions. The resulting global all sky climate feedback values are λ_{WVLR} =1.28 (1.13 to 1.45 at 66%) Wm⁻²K⁻¹, and λ_{albedo} =0.64 (0.53 to 0.74) Wm⁻² for the 2003-2023 period reducing to 0.35 (0.29 to 0.41) Wm⁻²K⁻¹ under 4°C warming after cryosphere retreat. Our findings agree well with complex Earth system model evaluations based on temporal climate perturbations, and our approach is complementary.

Plain Language Summary

The climate feedback measures how much Earth's surface temperatures will change in response to climate forcing from rising greenhouse gas concentrations. However, our observed record of surface temperature changes over time in response to rising greenhouse gas concentrations in the past is not long enough to accurately determine Earth's climate feedback for the future. In part, this limitation is because recent anthropogenic warming has only reached around 1 degree Celsius of temperature change globally so far. Here, we take an alternative approach: instead of considering how Earth's surface temperatures have changed over time we consider how Earth's surface temperatures change from the cold polar regions to the warm tropics which provides a much larger temperature change of around 80 degrees Celsius. By accounting for the different physical processes that affect Earth's surface temperature spatially, we are able to provide an estimate of the climate feedback in response to a climate forcing from greenhouse gas concentrations. Our spatial-change estimates of climate feedback are independent of the existing temporal-change estimates, but are in good agreement with current estimates of climate feedback.

1. Introduction

An imbalance in Earth's energy budget at the top of the atmosphere is eventually restored through climate feedback processes, whereby an increase in surface temperatures leads to an increase in outgoing radiation at the top of the atmosphere (TOA). The total climate feedback from all processes, λ_{total} in Wm⁻²K⁻¹, is defined as minus the partial derivative of outgoing radiation at the top of the atmosphere, R_{out} in Wm⁻²K⁻¹, with respect to surface temperature, T_S in K,

$$\lambda_{total} = -\frac{\partial R_{out}}{\partial T_S} \qquad . {1}$$

 λ_{total} for the present day Earth system is an important quantity in global climate science, since it is inversely linked to the Equilibrium Climate Sensitivity, ECS $\sim 1/\lambda_{total}$, and so determines the future surface warming response to some specified anthropogenic forcing. This total climate feedback may be decomposed into individual climate feedbacks from different processes, $\lambda_{total} = \sum \lambda_X$, where the feedback from process X is,

$$\lambda_X = -\frac{\partial R_{out}}{\partial T_S} \Big|_{\delta X} = -\frac{\partial [S_{out} + L_{out}]}{\partial T_S} \Big|_{\delta X} = -\frac{\partial [S_{out} + L_{out}]}{\partial X} \frac{\partial X}{\partial T_S} \quad , \tag{2}$$

where S_{out} is the outgoing shortwave radiation and L_{out} is the outgoing longwave radiation at the TOA. The different climate feedback processes, λ_X , include the Planck feedback, the water vapor-lapse rate (WVLR) feedback, the surface albedo feedback and cloud feedbacks; see Sherwood et al. (2020) for a comprehensive assessment.

 Existing studies quantify climate feedbacks (either as the total feedback or the separate contributions from individual processes) through temporal changes in surface temperatures and Earth's energy budget at the top of the atmosphere using either observations, numerical simulations or paleoclimate archives (e.g. Sherwood et al., 2020). However, temporal observations have only a limited historic record, especially for the energy budget, and the observed anthropogenic warming signal of around 1K is relatively small in comparison to the interannual variability and the uncertainty of the radiative effects of aerosols (Sherwood et al., 2020). Also, the climate feedback may have had a different mean value in recent historic decades than it does now due to how changing patterns of surface warming over time alter climate feedback, known as the pattern effect (see e.g. Gregory and Andrews, 2016).

Climate feedbacks are readily evaluated from numerical climate model simulations (e.g. Soden et al., 2008; Zelinka et al., 2020), which can use idealized forcing without aerosol contributions and simulate a longer time period than the historic record. While modern climate models include sophisticated representations of physical processes, the evaluated climate feedbacks do differ between different models (e.g. Zelinka et al., 2020), and so any single numerical model simulations may be biased relative to the real world. Also, if the goal is to evaluate the climate feedback contributions from different individual processes, λ_X , then the relatively large finite perturbations employed in numerical climate models lead to linear combination error in the individual feedbacks, such that $\lambda_{total} \neq \sum \lambda_X$ (e.g. the rms difference between λ_{total} and $\sum \lambda_X$

is 17.2 % for 27 CMIP6 models assessed by Zelinka et al., 2020, and 17.7 % for 28 CMIP5 models). Note that this nonlinear effect only impacts the values of λ_X for each process and does not impact the value of the total climate feedback, λ_{total} .

Consider an alternative approach based on the spatial variation in TOA outgoing radiation and surface temperature (Figure 1). Evaluated with 1° horizontal resolution during the 2003-2023 period, surface temperature correlates to TOA outgoing radiation and explains some 74 % of the variance in TOA outgoing radiation (Fig. 1), with a sensitivity of $\frac{\delta R_{out}}{\delta T_S} \approx 1.28 \text{ Wm}^{-2}\text{K}^{-1}$. This crude observational estimate is consistent in magnitude to recent estimates of climate feedback (e.g. $-\lambda_{total} = \partial R_{out}/\partial T_S = 1.30 \pm 0.44$ in Sherwood et al., 2020). However, it is not in general robust to assume that the value of $\delta R_{out}/\delta T_S$ analyzed spatially and the value of $\partial R_{out}/\partial T_S$ are similar: a significant part of the observed spatial variation in R_{out} may arise from factors that co-vary in space with T_S in recent climatology, but would not co-vary in time following a perturbation to the climate system. For example, Feng et al (2023a,b) reveal that some processes that contribute to how clear sky outgoing longwave radiation increases with surface temperature lead to a linear relationship (and so would also contribute in a similar manner spatially and temporally) but some processes lead to a departure from a linear relationship (and so would not act in a similar way temporally and spatially). These factors leading to departures from linearity, such as the mid-troposphere relative humidity (Feng et al., b), should be accounted for before making inferences on climate feedback from spatial information.

Previous studies in the literature have successfully related TOA outgoing radiation to parameters describing atmospheric and surface properties, either empirically or theoretically (e.g. Raval and Ramanathan, 1989; Koll and Cronin, 2018; Schmidt et al., 2010; Ingram, 2010), and so have described combinations of processes and parameters that explain variation in R_{out} . However, in general these empirically fitted relations for R_{out} are not easily differentiable with respect to surface temperature so cannot then be used to diagnose the climate feedback, (1).

The goal of this study is to evaluate climate feedbacks from the Planck, WVLR and surface albedo feedback processes using observations of the spatial variation in TOA outgoing radiation, surface temperature and other properties of the Earth's surface and atmosphere (where these other properties used in addition to surface temperature to help evaluate the climate feedbacks preferably vary independently of surface temperature). Spatial variation in observed surface temperature is of order 80 K (Fig. 1), thus providing a better signal-to-noise ratio than the much smaller order 1K temporal variation in observed surface temperature. To evaluate climate feedbacks, we first empirically relate R_{out} to T_S and other atmospheric and surface properties using functional forms that are easily differentiable with respect to surface temperature. The analysis is conducted on a 1° by 1° spatial resolution using climatology for the 2003-2023 period, evaluating feedbacks for both clear skies conditions and all skies conditions assuming constant cloud amount and cloud properties (i.e. fixed-cloud all sky conditions). Additional climate feedbacks associated with changes in cloud amount or cloud properties are not considered.

156

157

158159

160

161162

163

164165

166167

168

169

170

Recent studies have estimated climate feedbacks from theory and/or spatial variation in climate properties (e.g. Feldl and Merlis, 2023; Koll et al., 2023; Roemer et al., 2023). Feldl and Merlis (2023) use theory and spatial variation in climate properties to calculate climate feedback, but crucially the theory in their method does not solve for the radiative properties of the system, and instead employs radiative kernels (e.g. Soden et al., 2008) evaluated from model output forced with finite perturbations. Therefore, the Feldl and Merlis (2023) method does not provide an assessment of climate feedback terms that is independent of the numerical climate models. Koll et al. (2023) solves for a climate feedback term from first principles theoretically, and so does not require numerical model input, but solves for the longwave climate feedback under clear sky conditions only. The aim here is to solve for climate feedback terms involving Planck, WVLR and fixed-cloud albedo, each under both clear sky and all sky conditions, using theory applied to observational data for the climatological mean state. The climate feedbacks are solved independently of both numerical model output or time-varying climate signals. Note that fixed-cloud albedo includes both surface albedo and atmospheric albedo changes that are not caused by clouds (e.g. water vapor), while the WVLR feedback is explicitly a longwave-only feedback in this analysis.

Section 2 of this study derives and empirically fits new reduced physics, simplified relations describing variation in TOA outgoing radiation in terms of surface temperature and other surface and atmospheric properties. Section 3 then differentiates these simplified relations to evaluate the Planck, WVLR and fixed-cloud albedo climate feedbacks under clear sky and all sky conditions.

176 177

2. Simplified empirical relations for outgoing radiation at the TOA

178179

180

2.1 A framework for TOA outgoing radiation, planetary emissivity and planetary albedoA framework is adopted to derive the functional relationships where outgoing radiation under

sky condition i (signifying either clear-sky, cloudy-sky or all-sky conditions, where a cloudy sky is defined to have a cloud amount of 1 if cloud amount varies from 0 to 1) is related to the Stefan-

Boltzman constant, σ in Wm⁻²K⁻⁴, surface temperature, T_S , and incident solar radiation via, R_{in} , in Wm⁻², via,

185186

$$R_{out,i}(x,y) = L_{out,i}(x,y) + S_{out,i}(x,y) = \varepsilon_i(x,y)\sigma T_S^4(x,y) + \alpha_i(x,y)R_{in}(x,y)$$
(3)

187 188

189

where the planetary emissivity ε_i is defined by the outgoing longwave radiation at the top of the atmosphere as a fraction of the expected emitted radiation at the planet's surface for a black body averaged over some time span,

190 191

192
$$\varepsilon_i(x,y) = \int_t^{t+n\Delta t} \frac{L_{out,i}(x,y,t')}{\sigma T_S^4(x,y,t')} dt' / \int_t^{t+n\Delta t} dt' , \qquad (4a)$$

and the planetary albedo α_i in eq. (3) is defined as the outgoing shortwave radiation at the top of the atmosphere as a fraction of incident solar radiation at the top of the atmosphere averaged over some time span,

$$\alpha_i(x,y) = \int_t^{t+n\Delta t} \frac{S_{out,i}(x,y,t')}{R_{in}(x,y,t')} dt' / \int_t^{t+n\Delta t} dt'$$
 (4b)

2.1.1 Planetary emissivity

The definition of planetary emissivity adopted here, ε_i in eq. (4a), considers outgoing radiation measured at the top of the atmosphere and emitted radiation measured at the planet's surface. This planetary emissivity therefore accounts for both the direct emissivity effect of the surface material of the planet (where emitted radiation is less than σT_S^4) and the greenhouse effect of the atmosphere (where the atmosphere both absorbs and re-emits longwave radiation so that the outgoing longwave radiation at the top of the atmosphere is less than the upward longwave radiation at the planet's surface). Note that the Sherwood et al. (2020) climate feedback review also utilizes the same planetary emissivity definition when analyzing the Planck feedback.

The climatological monthly mean clear sky planetary emissivity, $\varepsilon_{ClearSky}(x,y)$, for the period 2003-2023 varies spatially from 0.57 to 1.0 (Fig. 2, left hand column), with low values in tropical regions and high values near the poles. This range of values implies that atmospheric absorption and emission of radiation and surface emissivity properties reduce the top of the atmosphere outgoing longwave radiation, relative to the expected longwave blackbody radiation emitted by the Earth's surface, by up to 43 % under clear skies. In all sky conditions, monthly mean planetary emissivity, ε_{AllSky} , varies spatially from 0.39 to 1.0, such that in the presence of clouds outgoing longwave radiation at the top of the atmosphere is reduced by up to 61 % relative to the expected surface emission by a blackbody.

2.1.2 Planetary albedo

The definition of planetary albedo definition adopted here, α_i in eq. (4b), considers incident and reflected radiation both measured at the top of the atmosphere. This planetary albedo definition therefore accounts for the shortwave radiation reflection both by the planet's surface and by atmospheric constituents in either clear sky, cloudy sky or all sky conditions. The monthly climatological planetary albedo varies spatially from <0.10 to 0.88 in clear sky conditions and 0.10 to 0.96 in all sky conditions (Fig. 3).

2.1.3 Differential forms for planetary emissivity and planetary albedo

From eq. (3) we can see that the TOA outgoing shortwave radiation is related to incoming solar radiation by $S_{out,i}(x,y) = \alpha_i(x,y)R_{in}(x,y)$ and the TOA outgoing longwave radiation is related to the expected blackbody emission at the Earth's surface by $L_{out,i}(x,y) = \varepsilon_i(x,y)\sigma T_S^4(x,y)$ under sky condition i. The values of planetary albedo and planetary emissivity vary spatially (Figs. 2, 3) and with surface temperature (Fig. 4). The goal is therefore to identify reduced physics simplified relations for α_i and ε_i that are differentiable with respect

to surface temperature to identify the Planck, WVLR and fixed-cloud albedo climate feedbacks in clear sky and all sky conditions.

237 238 239

240

241

242

243

236

In order to be differentiable with respect to surface temperature to evaluate the climate feedback, the simplified relations that solve for TOA outgoing shortwave and longwave radiation, via solving for α_i and ε_i , must only contain parameters that are relatively insensitive to perturbations in surface temperature. Consider two simplified functions where planetary emissivity is related to surface temperature and I other parameters describing the atmospheric and surface properties,

244 245 246

$$\varepsilon_i = f(T_S, x_1, x_2 \dots x_I) \tag{5a}$$

247 248

and planetary albedo is related to surface temperature and K other properties,

249 250

$$\alpha_i = g(T_S, y_1, y_2 \dots y_K) \tag{5b}$$

251

- Ideally, we should like all other parameters to be orthogonal to T_S under climate perturbation 252
- so that so that we are to differentiate these functions, f and g, with respect to surface 253
- temperature without knowing the sensitivity of each separate parameter to T_S , $\frac{\partial x_j}{\partial T_S}$. Given that 254
- we may not be able to identify parameters that are perfectly orthogonal to T_S and still 255
- accurately capture the variation in ε_i and α_i , then we require: 256

257

260 261

259

for each of the
$$J$$
 parameters that are not $T_{\mathcal{S}}$ in the emissivity relation (5a) and

$$262 \qquad \left| \frac{\partial \alpha_i}{\partial T_S} \right| \gg \left| \frac{\partial y_k}{\partial T_S} \frac{\partial \alpha_i}{\partial y_k} \right| \tag{6b}$$

263 264

265

- for each of the K parameters that are not T_S in the albedo relation (5b). Therefore, here we cannot use parameters such as total precipitable column water vapor or specific humidity, since these parameters vary significantly over time with a surface temperature perturbation. For
- example, if x_{i} were precipitable water vapor column then after temperature increase x_{j} would 267
- also increase, $\frac{\partial x_j}{\partial T_s} > 0$, since warm air holds more water vapor. This increase in precipitable 268
- water vapor column then reduces planetary emissivity, $\frac{\partial \varepsilon_i}{\partial x_i} < 0$, from the greenhouse effect. 269
- Therefore the magnitude $\left| \frac{\partial x_j}{\partial T_S} \frac{\partial \varepsilon_i}{\partial x_j} \right|$ could be considerable, and break condition (6a). However, 270
- instead we can use parameters such as surface relative humidity and the height of the 271
- tropopause (that are related to specific humidity and total precipitable water vapor content), 272
- since the changes in these quantities over time after temperature perturbation have a greater 273
- chance of satisfying condition (6a) and (6b). For example, if x_i were relative humidity then x_i 274

275 would not likely change significantly with surface warming, $\frac{\partial x_j}{\partial T_S} \sim 0$, and so $\left| \frac{\partial x_j}{\partial T_S} \frac{\partial \varepsilon_i}{\partial x_j} \right|$ would satisfy condition (6a).

277278279

2.1.4 Clear sky, cloudy sky and all sky conditions

- In clear sky conditions, the 2003-2023 annual-mean climatology evaluated planetary emissivity,
- 281 $\varepsilon_{ClearSky}$, is nearly linearly related to surface temperature (Fig. 4e): $\frac{\delta \varepsilon_{ClearSky}}{\delta T_S} = -3.75 \text{ K}^{-1} \text{ with}$
- 282 R² of 0.96 (see Koll and Cronin, 2018). The 2003-2023 annual-mean climatology evaluated clear
- 283 sky planetary albedo, $\alpha_{ClearSky}$ (Fig. 4f), shows a non-linear relationship to surface temperature
- with generally high albedo for annual-mean temperatures below 260 K (cold enough for the
- cryosphere to persist much of the year) and generally low albedo for annual-mean
- temperatures above 270 K (too warm for the cryosphere). Some locations with temperatures
- above 290 K show increased albedo, reflecting hot dry dessert regions over land with low plant
- coverage. Since climate feedbacks are related to the partial derivative of outgoing radiation
- with respect to surface temperature (eqs. 1, 2), this study aims to identify the partial
- derivatives, $\frac{\partial \varepsilon_{ClearSky}}{\partial T_S}$, $\frac{\partial \varepsilon_{AllSky}}{\partial T_S}$, $\frac{\partial \alpha_{ClearSky}}{\partial T_S}$ and $\frac{\partial \alpha_{AllSky}}{\partial T_S}$ through observation-constrained
- 291 functional relationships that are used to extract the impact of any factors that co-vary spatially
- with surface temperature in recent climatology (Fig. 4). The values of $\frac{\partial \alpha_{ClearSky}}{\partial T_S}$ and $\frac{\partial \alpha_{AllSky}}{\partial T_S}$ will
- 293 necessarily come from non-linear functions that approximate the non-linear relation between
- 294 $\alpha_{ClearSky}$ and T_S (Fig. 4f).

295

The planetary emissivity and albedo for the three different sky conditions, all sky, clear sky and cloudy sky, are connected via,

298

299
$$\varepsilon_{AllSky}(x,y) = f_{CA}(x,y)\varepsilon_{CloudySky}(x,y) + [1 - f_{CA}(x,y)]\varepsilon_{ClearSky}(x,y)$$
 (7a)

300 and

301

$$\alpha_{AllSky}(x,y) = f_{CI}(x,y)\alpha_{CloudySky}(x,y) + [1 - f_{CI}(x,y)]\alpha_{ClearSky}(x,y)$$
(7b)

- where f_{CA} is the cloud amount area fraction and f_{CI} is the cloud incident radiation fraction.
- Note that when averaging over time the cloud incident radiation fraction may differ from the
- 305 cloud amount area fraction, and is calculated via

306

$$f_{CI}(x,y) = \frac{\sum f_{CA}(x,y,m)R_{in}(x,y,m)\Delta t_m}{\sum R_{in}(x,y,m)\Delta t_m}$$
(8)

308309

where m is some time interval.

- Section 2.1 considers the planetary emissivity and albedo in clear sky conditions, while section
- 2.2 explores the impact of clouds in modifying the planetary emissivity and albedo in all sky
- 313 conditions.

2.2 TOA outgoing radiation in clear skies

2.2.1 Outgoing Shortwave radiation for Clear Sky

Simplified functional relationships are now assessed for clear sky planetary albedo, $\alpha_{ClearSky}$, in terms of surface temperature and other properties of the climate system. Here, we allow clear sky planetary albedo to be a function of surface temperature T_s , whether the surface is land or ocean, k, and latitude ϕ ,

$$\alpha_{ClearSky} \approx f(T_s, k, \phi)$$
 (9)

where the explicit latitudinal dependency on ϕ is assumed to arise solely due to the geometrical effect of changes in mean annual solar zenith angle. The temperature effect on $\alpha_{ClearSky}$ in (9) is assumed to implicitly represent both changes to the surface albedo through the cryosphere and changes to clear sky albedo from changing clear sky atmospheric properties, for example changes in the amount of water vapour altering the absorption and scattering of shortwave radiation (e.g. Pincus et al., 2015). The impacts of this implicit simplification on the results are discussed below. Observations reveal how monthly-climatology $\alpha_{ClearSky}$ varied seasonally and spatially during the period 2003-2023 (Fig. 3), with generally high values for high-latitude snow and ice covered regions and lower values over sea and vegetation-covered land regions. The annual-mean values of local clear sky planetary albedo for the 2003-2023 climatology, $\alpha_{ClearSky}$, reflect differences due to annual mean surface temperature, latitude and whether the local region is land or sea (Fig. 5a, grey and green). The monthly mean albedo values are converted to annual means using insolation-weighting, so at high latitudes the summer months contribute more to the annual mean, in line with the mean solar-zenith angle arguments of Cronin (2014).

Now consider the functional forms for annual-mean albedo at some specified spatial coordinates in terms of latitude and surface temperature over land and ocean, eq. (9). First, we seek to explore the latitudinal dependence, ϕ , and then later the temperature dependence, T_s , for land and ocean, t_s . The latitudinal dependence of albedo is assumed to arise due to the change in solar zenith angle affecting the amount of incident light reflected at any given time, and across a year. The annual-mean planetary albedo for surface-type t_s at latitude t_s 0, t_s 1 is assumed to be related to the planetary-mean albedo for a planet covered entirely by the same surface-type t_s 1, t_s 2, via a relation containing a second order Legendre polynomial in t_s 3 in t_s 4 after Goodwin and Williams (2023), with an additional coefficient added here, t_s 3, giving,

$$\alpha_j(\phi) = \left[1 + \left[1 - \overline{\alpha}_j \right] \beta \left[\frac{1}{2} \left[3 \sin^2 \phi - 1 \right] \right] \right] \overline{\alpha}_j \tag{10}$$

The additional coefficient β is a tunable parameter within the range $0 \le \beta \le 1$, where 0 indicates no latitudinal dependence on albedo for surface-material j due to latitudinal geometry and 1 indicates the maximum possible latitudinal dependence. Note that when both

constraints $0 \le \beta \le 1$ and $0 \le \overline{\alpha}_j \le 1$, eq. (10) implies physically plausible values for local albedo, $0 \le \alpha_j(\phi) \le 1$, for all ϕ . The second order Legendre polynomial sine of latitude is able to accurately account for how the annual-mean solar zenith angle by the Earth with latitude (e.g. Hartmann, 1994), providing some confidence for its application (with altered coefficients) to account for how annual-mean solar zenith angle affects albedo with latitude (Goodwin and Williams, 2023).

The annual-mean local albedo is generally higher for cold regions that are covered in snow and ice most or all of the year and have lower water vapor levels, and generally lower for warmer regions that are ice- and snow-free for most of the year and have higher water vapor levels (Fig. 5a). Applying eq. (10) to each annual-mean local albedo value (α_j : Fig. 3a) would then reveal the effective planetary-mean albedo for a planet entirely covered by the surface material found at that location ($\overline{\alpha_j}$). This approximation is assumed here to effectively strip away the latitudinal impact on local fixed-cloud albedo, and leave only the temperature and land or ocean factors. To do this, we must first identify an approximate functional relationship between temperature and $\overline{\alpha_j}$ for land and ocean that will then be empirically constrained.

How should temperature impact clear sky albedo? Here, we assume that when the ocean is warm enough to be ice-free all year, then increasing the temperature further has no impact on local albedo. Therefore, the reduction in local albedo over the ocean as temperatures warm from 280 K to 300 K is assumed here to be a latitudinal geometry effect arising from variation in mean annual solar zenith angle (Fig. 5a, grey), consistent with previous observational analysis of sea surface albedo with solar zenith angle (Payne, 1972). Similarly, we assume that when the land is cold enough to be ice-covered all year, that reducing the temperature further has no impact on local albedo. Therefore, the increase in local albedo when annual land temperatures reduce from 245 K to 220 K (Fig. 5a, green) is assumed here to be a latitudinal geometry effect. We seek a functional form that, on an $\overline{\alpha}_J$ - T_S plot has a low dependence at high and low temperatures, with high $\overline{\alpha}_J$ at low T_S and low $\overline{\alpha}_J$ at high T_S , and has a continuous and differentiable form between these limiting values (e.g. Fig. 5b, lines).

The temperature dependence of the planetary albedo for a planet entirely covered by either land or ocean, $\overline{\alpha_{ClearSky,k}}$, is assumed to be represented by a relation containing the error function with respect to annual mean surface temperature via (e.g. Fig. 5b, lines)

$$\overline{\alpha_{ClearSky,k}}(T_S) = \left(\frac{\overline{\alpha_{warm,k}} + \overline{\alpha_{cold,k}}}{2}\right) - \left(\frac{\overline{\alpha_{cold,k}} - \overline{\alpha_{warm,k}}}{2}\right) \operatorname{erf}\left(\frac{T_S - (T_{warm,k} + T_{cold,k})/2}{(T_{warm,k} - T_{cold,k})/2}\right)$$
(11)

where k indicates either land or ocean, $\overline{\alpha_{warm,k}}$ is the planetary mean albedo covered in surface k held at temperatures with no snow or ice, $\overline{\alpha_{cold,k}}$ is the planetary mean albedo for surface k held at temperatures where there is snow or ice all year, $T_{warm,k}$ is the annual mean temperature above which the surface has very little snow or ice at any time of year, and $T_{cold,k}$ is the annual mean temperature below which the surface is almost entirely snow or ice covered all year.

The latitudinal dependence on clear sky planetary albedo is then modelled using a second order Legendre polynomial (eq. 10) to convert $\overline{\alpha_{ClearSkv,k}}$ to $\alpha_{ClearSkv}$,

$$\alpha_{ClearSky}(x, y, T_S) = \left[1 + \left[1 - \overline{\alpha_{ClearSky}}(x, y, T_S)\right]\beta \left[\frac{1}{2}\left[3\sin^2\phi - 1\right]\right]\right]\overline{\alpha_{ClearSky}}(x, y, T_S)$$
(12)

Closures (10) and (11) have tunable parameters β , $\overline{\alpha_{warm,land}}$, $\overline{\alpha_{cold,land}}$, $\overline{\alpha_{warm,ocean}}$, $\overline{\alpha_{cold,ocean}}$, $T_{warm,land}$, $T_{cold,land}$, $T_{warm,ocean}$ and $T_{cold,ocean}$. These parameters are tuned to minimize the root of mean squares error in how eqs. (10) and (11) estimate $\alpha_{ClearSky}(x,y,T_S)$ from observed climatology (Table S1; Fig. 5b, compare lines to dots). This is achieved in two stages: first the values of the parameters are fitted to $\alpha_{ClearSky}(x,y,T_S)$ over land for all land points with $T_S < 290$ K (since we are not attempting to include desertification at high temperatures within out scheme, Fig. 5a, green). Secondly, the the values of the parameters are fitted for the ocean assuming that $\overline{\alpha_{cold,k}}$ and β are the same for the ocean as the land (as the lack of data points with very low temperatures above the ocean, Fig. 5a, grey, makes $\overline{\alpha_{cold,ocean}}$ and in turn β difficult to fit, and very low temperatures are assumed to be entirely ice or snow covered all year regardless of whether they are over land or ocean).

These relations, eqns. (10-12) with the tuned values of β , $\overline{\alpha_{warm,land}}$, $\overline{\alpha_{cold,land}}$, $\overline{\alpha_{warm,ocean}}$, $\overline{\alpha_{cold,ocean}}$, $T_{warm,land}$, $T_{cold,land}$, $T_{warm,ocean}$ and $T_{cold,ocean}$ (Table S1), predict the clear sky albedo over each 1°x1° surface location based on the annual mean surface temperature (Fig. 5b, compare lines to dots). The statistical models (eqns. 10, 11; Fig. 5b, compare lines to dots) have R²=0.962 for $\alpha_{ClearSky}(x,y,T_S)$ over the ocean and R²=0.949 over land ($T_S < 290$ K), and predict $\alpha_{ClearSky}(x,y,T_S)$ values with a root mean square error of 0.0268 over the ocean and 0.0486 over land with $T_S < 290$ K (Fig. 3). Note that variation in atmospheric aerosol loading are not considered in the equations, and will lead to scatter between observed and empirically constrained values (Fig. 5b). The annual clear sky albedo $\alpha_{ClearSky}(x,y,T_S)$ ranges from 0.09 to 0.70 and is spatially well predicted from T_S , k and ϕ by the empirical relations (eqns. 9-12; Fig. 3, top row) with an overall r.m.s. error of 0.04. The largest local errors on land arise in desert and grassland regions, which have higher local clear sky albedo than other land regions at the same temperature, and in the ocean arise at the northernmost edge of the Southern Ocean sea-ice extent, where local clear sky albedo is slightly underestimated in the empirical predictions (Fig. 3).

The functions adopted here to describe the latitudinal and temperature impacts on clear sky albedo (eqns. 10, 11) are reasonable since:

(1) The single fitted value of $\beta=0.33\pm0.01$ produces the correct equatorial to high-latitude variation in *clear sky* albedo over the ocean (Fig. 3, top row, consider regions warm enough to remove any significant sea ice) and the correct equatorial to high-latitude variation in *sea surface* albedo in the Atlantic Ocean analyzed by Payne (1972) (see Supporting Information S3: Payne (1972) observes annual equatorial sea surface albedo of 0.06 increasing to between 0.08 and 0.10 for +60° to +70° latitude, in line with eq. (10) using $\beta=0.33$ and $\overline{\alpha}_j$ tuned to give equatorial albedo of 0.06). This agreement indicates that the latitudinal variation observed is

- explainable primarily due to a solar zenith angle geometry affecting the planetary surface 440
- reflection as assumed in the equations, and not a latitudinal variation in atmospheric 441
- 442 absorption since this does not affect sea surface albedo;
- (2) The single fitted value of $\beta = 0.33 \pm 0.01$ removes any significant slope in planetary clear 443
- sky albedo with temperature at both warm locations, for ocean and land, and cold locations, 444
- 445 over land (compare Fig. 5b to Fig. 5a, green and grey dots), showing that the latitudinal
- geometry impact on local clear sky albedo is accurately accounted for across different surface 446
- 447 types; and
- (3) The fitted parameter values (Table S1) are able to accurately calculate the planetary albedo 448
- calculated for each location with low rms error (Fig. 5b, compare lines to dots), showing that 449
- the surface temperature impact on albedo is accurately accounted for. 450

- There is more error in the land reconstruction than for the ocean, in part since the land has 452
- 453 very warm regions that are dry and so have low vegetation and high albedo (Fig. 5). The
- 454 functional equations chosen are only intended to account for the cryosphere impact on albedo
- 455 with temperature, not the impact from the drying out of soils and changing of the vegetation
- 456 state.

457

- The annual mean clear sky albedo $\alpha_{ClearSky}$ ranges from 0.09 to 0.70 (Fig. 5a), while the 458
- implied global annual mean clear sky albedo if the entire planet was covered in that surface 459
- material $\overline{\alpha_{ClearSky}}$ ranges from 0.10 to 0.66 (Fig. 5b). The range in $\alpha_{ClearSky}$ is due to both 460
- surface temperature (via the cryosphere extent and atmospheric water vapor) and solar zenith 461
- angle, while $\overline{\alpha_{ClearSky}}$ has the solar zenith angle effect removed. The reduced range in 462
- $\overline{\alpha_{ClearSky}}$ compared to $\alpha_{ClearSky}$ implies that some 91% of the observed range in clear sky 463
- albedo is functionally related to surface temperature, while 9% is due to variation in factors 464
- 465 that co-vary with temperature in space but would not co-vary with surface temperature in time following perturbation, such as the solar zenith angle change with latitude.
- 466

467 468

469

470

471

472

2.2.2 Outgoing Longwave radiation for Clear Sky

Simplified functional relationships are now assessed for clear sky planetary emissivity in terms of surface temperature and other climate properties. Based on simple physical considerations, we expect that clear sky planetary emissivity, $\varepsilon_{ClearSky}$, will decrease with:

- an increase in surface temperature T_S , since warmer air holds more water vapor;
- an increase in mid-troposphere relative humidity H_{rel} , since water vapor is a greenhouse 473 474 gas (see Feng et al. (2023b) for discussion of why outgoing longwave radiation is best related to the average mid-troposphere relative humidity, from 250 to 750 hPa); 475
- an increase in the height of the tropopause above the surface, $z_{trop} z_s$, since a higher 476 477 tropopause indicates that water vapor extends to a greater height in the atmosphere and 478 reflects changes to the lapse rate;
- an increase in surface pressure, p_s , since this indicates a greater mass of atmosphere above 479 the surface, and so greater greenhouse effect. 480

Based on these physical considerations, we postulate a simplified linearized relationship whereby planetary emissivity is linearly related to surface temperature, T_S ; relative humidity in the mid-troposphere (250-750 hPa: Feng et al., 2023b), H_{rel} ; the height of the tropopause above local surface elevation, $z_{trop}(x,y,t)-z_s(x,y)$; and surface pressure, p_s , via,

487
$$\varepsilon_{ClearSky}(x, y, t)$$

488 $\approx c_o + c_1 T_S(x, y, t) + c_2 H_{rel}(x, y, t) + c_3 [z_{trop}(x, y, t) - z_S(x, y)]$
489 $+ c_4 p_S(x, y, t)$
490 (13)

For monthly mean observed climatology from 2003-2023 on a 1° by 1° spatial resolution, the coefficients for eq. (13) are fitted (Table S2). The empirically constrained simplified relation calculates $\varepsilon_{ClearSky}(x,y,t)$ across all 12 months and each 1° by 1° location with a root of mean squares error of 0.0248, and has an adjusted R² value of 0.906, thus providing accurate monthly spatial estimates of planetary clear sky emissivity (Fig. 2, top two rows). In addition to producing predictions in agreement observations (Fig. 2), if the simple physical justification for eq. (13) holds then we should also expect that the empirically fitted coefficient values c_1 , c_2 , c_3 and c_4 should all be negative, which they are (Table S2). Note that additional processes may affect how vertical temperature structure and outgoing longwave radiation change over time but are not considered in this methodology (i.e. a lapse rate component of the feedback that is not linked to changes in tropopause height). Such processes would alter $\varepsilon_{ClearSky}(x,y,t)$ over time in a way that is not captured by eq. (13). The applicability of eq. (13) for spatial variation is supported by results from Feng et al. (2023a), who find that the vertical temperature structure (lapse rate) is not of primary importance in varying outgoing longwave radiation spatially.

The coefficient c_1 takes the value $c_1 = \frac{\partial \varepsilon_{ClearSky}}{\partial T_S} = -(-2.904 \pm 0.003) \times 10^{-3} \text{ K}^{-1}$ when (13) is empirically fitted to data on a monthly climatological basis (Supplementary Table S2), indicating that 77% of the observed spatial variation in $\varepsilon_{ClearSky}$ with T_S ($\frac{\delta \varepsilon_{ClearSky}}{\delta T_S} = -3.75 \times 10^{-3} \text{ K}^{-1}$: Fig. 4e) is functionally due to variation in surface temperature, whereas 23% of the observed variation is due to variation in factors that co-vary with temperature in space but would not covary with surface temperature in time following perturbation. For example, spatial locations with high surface elevation and low surface pressure are generally also cold and have high planetary emissivity, $\varepsilon_{ClearSky}$. There is also a near-linear relationship between L_{out} and T_S in the region of parameter space considered (Fig. 2c,e), implying that up to around 77% of the spatial variation in outgoing longwave radiation at the top of the atmosphere is functionally related to surface temperature. See also Feng et al. (2023b) for explanation of the reasons behind outgoing longwave radiation's near linear temperature dependence and its non-linear component.

2.3 TOA outgoing radiation in all sky conditions

2.3.1 Outgoing Shortwave for All Sky

Now, the impact of clouds on the planetary albedo is assessed to constrain a relation for albedo feedback under all sky conditions. The albedo of clouds is evaluated using a model of how clouds either reflect or emit radiation, and the surface of the planet reflects radiation, leading to an infinite series of emission and reflection contributions (Supporting Information Text S1 and Fig. S1). A key difference relative to previous infinite series models (e.g. Taylor et al., 2007) is that here a distinction is made between the albedo of cloud for *directed* incident solar radiation (which is assumed to be latitudinally dependent due to changes in mean solar zenith angle) and the albedo of cloud for *diffuse* upwards radiation that has been reflected by the Earth's surface (which is assumed to be latitudinally independent). This difference in albedo

between directed and diffuse light arises because the angle of incidence affects the albedo (e.g.

- **Stephens, 1978).**
- Adopting this separation of directed and diffuse albedo model (Supporting Information Text S1 and Fig. S1), the cloudy sky albedo is related to the clear sky albedo via,

$$\alpha_{CloudySky}(x,y) \approx \alpha_{Cloud:dir}(x,y) + \overline{\alpha_{ClearSky}}(x,y) \frac{[1 - \alpha_{Cloud:dir}(x,y)][1 - \overline{\alpha_{Cloud}}]}{[1 - \overline{\alpha_{ClearSky}}(x,y) \times \overline{\alpha_{Cloud}}]}$$
(14)

- where $\alpha_{Cloud:dir}(x,y)$ is the annual mean albedo of cloud at location x,y for directed incident solar radiation, $\overline{\alpha_{Cloud}}$ is the global mean cloud albedo, which is assumed equal to the albedo of cloud for diffuse radiation from below and is invariant with latitude. Using observational estimates for $\alpha_{CloudySky}(x,y)$ (Fig. 3) and modifying observed $\alpha_{ClearSky}(x,y)$ with eq. (12) to obtain $\overline{\alpha_{ClearSky}}(x,y)$, eq. (14) is iteratively solved to calculate the climatological spatial pattern of cloud albedo for directed solar radiation, $\alpha_{Cloud:dir}(x,y)$, for the period 2003-2023 (Figure 6, right hand column), noting that $\overline{\alpha_{Cloud}}$ is the global average cloud albedo.
- The local variations in reconstructed cloud albedo, $\alpha_{Cloud:dir}$, reflect differences in cloud properties (Fig. 6). However, within this variation due to local cloud properties, the evaluated values of $\alpha_{Cloud:dir}(x,y)$ show a general pattern of increasing with latitude ϕ (Fig. 6, right hand side), consistent with the Stephens (1978) theoretical model and parameterization identifying how the magnitude of cloud albedo varies with solar zenith angle (see Stephens, 1978, Figure 4 therein).

2.3.2 Outgoing Longwave for All Sky

- Now, the impact of clouds on the relationship between clear sky planetary emissivity and surface temperature is considered. Clear sky planetary emissivity $\varepsilon_{ClearSky}$ is empirically related to surface temperature via equation (13). However, to calculate longwave climate feedbacks in all sky conditions, we need to relate planetary emissivity in all sky conditions, ε_{AllSky} , to $\varepsilon_{ClearSky}$.
- With no atmosphere, and a perfect blackbody surface, the planetary emissivity would be equal to 1. In clear sky conditions planetary emissivity is less than 1 because greenhouse gasses in the atmosphere reduce the TOA outgoing longwave radiation compared to the expected emission

from the surface (Fig. 2, left hand column): the ambient reduction in planetary emissivity in clear sky conditions is $1 - \varepsilon_{ClearSky}$. This ambient planetary emissivity is reduced further in the presence of clouds because clouds themselves reduce TOA outgoing radiation (Fig. 2, compare middle and left hand columns): the total reduction in planetary emissivity with clouds and an atmosphere is $1 - \varepsilon_{CloudySky}$ (Supplementary Figure S2).

 Since clouds reduce outgoing longwave radiation at the TOA, a recent study (Goodwin and Williams, 2023) expressed this reduction of planetary emissivity due to clouds of clouds via a cloud-emissivity coefficient, $c_{\varepsilon} = \left[1 - \varepsilon_{CloudySky}\right]/\left[1 - \varepsilon_{ClearSky}\right]$, where c_{ε} is an amplification factor by which the value of one minus the emissivity for clear sky conditions is amplified in cloudy sky conditions. The value of c_{ε} represents the impact of clouds on the longwave radiation budget and varies with cloud type.

Here, we utilize this cloud-emissivity coefficient to relate ε_{AllSky} to $\varepsilon_{ClearSky}$ and parameters representing cloud amount, f_{CA} , and cloud type, c_{ε} , of the form

$$\varepsilon_{AllSky} = \varepsilon_{ClearSky} - f_{CA}(c_{\varepsilon} - 1) (1 - \varepsilon_{ClearSky})$$
(15)

where the cloud-emissivity coefficient (Goodwin and Williams, 2023) expresses the longwave radiation budget impact of clouds via,

$$c_{\varepsilon}(x,y,t) = \frac{\left[1 - \varepsilon_{CloudySky}(x,y,t)\right]}{\left[1 - \varepsilon_{ClearSky}(x,y,t)\right]} \tag{16}$$

Here, the cloud emissivity coefficient of Goodwin and Williams (2023), is re-analyzed for the 2003-2023 period, using monthly climatology at 1° by 1° spatial resolution (Fig. 6, left hand panels). The resulting values of c_{ε} for across each 1° by 1° gridpoint in each month have a median value of $c_{\varepsilon}=1.23$, 66% of values between 1.11 and 1.34 and 90% of values between 1.05 and 1.42 (Fig. 6, left hand panels). Therefore, the value of $1-\varepsilon_{CloudySky}$ is larger than $1-\varepsilon_{ClearSky}$ by between 5 and 42% across spatial and monthly variation for 90% of the time. Note that the variation in c_{ε} values arises for local climate states with very different monthly climatologies, with large variation in surface temperatures, relative humidites, surface elevations and other climatological parameters including cloud type.

 Combining the empirical prediction for clear sky planetary emissivity ($\varepsilon_{ClearSky}$; eq. 13; Fig. 2) with the observed spatial monthly climatology for the cloud emissivity coefficient (c_{ε} ; eq. 16; Fig. 6), and accounting for observed cloud amount using eq. (7a), produces an empirical relation for all sky planetary emissivity, $\varepsilon_{AllSky}(x,y,t)$ (eq. 15; Figure 2, bottom two rows), where the empirical prediction in Fig. 2 uses $\varepsilon_{ClearSky}$ values predicted from eq. (13) and f_{CA} and c_{ep} as observed from monthly climatology. This empirical prediction for spatial and monthly all sky emissivity is in good agreement with the observed values (Fig. 2), with an r.m.s. error of 0.03 (Fig. 2, bottom two rows). There is significant local error in isolated cold polar locations where $\varepsilon_{ClearSky}(x,y,t)$ is close to 1, and the denominator of eq. (16) goes to zero.

611

3. Climate feedbacks

The simplified functional relationships for planetary emissivity and planetary albedo to calculate the Planck, WVLR and albedo climate feedbacks in clear sky and all sky conditions are now utilized. Cloud feedbacks are not considered. From eqns. (1), (2) and (7), the local climate feedback for sky-condition i at location x, y is defined as,

616

$$\delta_{i}(x,y) = -\frac{\partial R_{out,i}}{\partial T_{S}}(x,y) = -\frac{\partial}{\partial T_{S}} \left[\varepsilon_{i}(x,y) \sigma T_{S}^{4}(x,y) + \alpha_{i}(x,y) R_{in}(x,y) \right]$$
 (17a)

618

619 which differentiates giving,

620

$$\lambda_{i}(x,y) = -\underbrace{4\varepsilon_{i}(x,y)\sigma T_{S}^{3}(x,y)}_{Planck} - \underbrace{\sigma T_{S}^{4}(x,y)\frac{\partial\varepsilon_{i}}{\partial T_{S}}(x,y)}_{WVLR+LWcloud} - \underbrace{R_{in}(x,y)\frac{\partial\alpha_{i}}{\partial T_{S}}(x,y)}_{albedo+SWCloud}$$
(17b)

622

- To remove the cloud feedbacks from eq. (17) we set in this study the partial derivatives of
- emissivity and albedo with surface temperature to be evaluated without a temporal change in
- cloud amount, cloud emissivity coefficient or cloud albedo, such that $\frac{\partial \varepsilon_i}{\partial T_s} =$
- $\frac{\partial \varepsilon_i}{\partial T_S} \bigg|_{\delta f_{CA} = \delta c_\varepsilon = \delta \alpha_{Cloud} = 0} \text{ and } \frac{\partial \alpha_i}{\partial T_S} = \frac{\partial \alpha_i}{\partial T_S} \bigg|_{\delta f_{CA} = \delta c_\varepsilon = \delta \alpha_{Cloud} = 0}.$ The consequences of changes in cloud
- amount and cloud properties (via cloud emissivity coefficient and cloud albedo) with time are
- 628 reserved for future study.

629

Analyzing the global mean climate feedback for some process and cloud state $\overline{\lambda_i}$ then requires convoluting this spatial feedback (eq. 17) with a warming pattern,

632

633
$$\overline{\lambda}_{l} = \frac{\int \lambda_{l}(x,y)\Delta T_{S}(x,y)dxdy}{\int \Delta T_{S}(x,y)dxdy}$$
 (18)

634

- Here, we use the multi-model warming pattern for a 2°C global-mean warming from
- 636 Assessment Report 6 of the Intergovernmental Panel on Climate Change (IPCC, 2021). The
- associated 4°C warming pattern (IPCC, 2021) is also used to assess how climate feedbacks vary
- 638 with the background climate state, by re-analyzing the climate feedback for surface
- temperature profiles of +2 K and +4 K warming (calculated as the ERA5 temperature profile for
- 1940-1960 with the +2 K and +4 K IPCC (2021) warming patterns).

641642

3.1 Planck feedback

- The Planck feedback is defined here as the change in outgoing radiation following a change in
- surface temperature while atmospheric planetary emissivity is held constant (to represent
- constant atmospheric constituents). The Planck feedback for clear skies is written, from eq.
- 646 (11),

$$\lambda_{Planck,ClearSky}(x,y) = -4\varepsilon_{ClearSky}(x,y)\sigma T_S^3(x,y)$$
(19)

while the Planck feedback for all sky conditions is,

651652

$$\lambda_{Planck,AllSky}(x,y) = -4\varepsilon_{AllSky}(x,y)\sigma T_S^3(x,y)$$
 (20)

653654

- Using monthly mean climatology for the period 2003-2023, the Planck feedback is analyzed,
- giving a global spatial average of $\lambda_{Planck,ClearSky} = -3.72 \text{ Wm}^{-2}\text{K}^{-1}$ and $\lambda_{Planck,AllSky} = -3.33$
- 657 Wm⁻²K⁻¹ for uniform surface warming. When convoluted with a multi-model mean pattern for
- 2°C global warming (IPCC, 2021), the 2003-2023 all sky Planck feedback becomes
- $\lambda_{Planck,AllSky} = -3.30 \text{ Wm}^{-2}\text{K}^{-1}$. This Planck feedback analysis is similar to previous methods
- (e.g. see Sherwood et al., 2020), and correspondingly gives similar results (Table 1).

661 662

3.2 Clear sky and fixed-cloud all sky planetary albedo feedback

The clear-sky albedo feedback is written, from eq. (17),

663 664

$$\lambda_{albedo,ClearSky}(x,y) = -R_{in}(x,y) \frac{\partial \alpha_{ClearSky}}{\partial T_S}(x,y)$$
 (21)

666

- The clear sky planetary albedo feedback, $\lambda_{albedo,ClearSky}(x,y)$, is now evaluated by
- differentiating $\alpha_{ClearSky}$ with respect to surface temperature and substituting into the relevant
- term in eq. (17). The partial derivative of local clear sky albedo respect to surface temperature
- 670 is evaluated via,

671

672
$$\frac{\partial \alpha_{ClearSky}}{\partial T_S}(x,y) = \left[1 + \beta \left[\frac{1}{2} \left[3 \sin^2 \phi - 1\right]\right]\right] \frac{\partial \overline{\alpha_{ClearSky}}}{\partial T_S}(x,y)$$
 (22)

673

- where $\frac{\partial \overline{\alpha_{ClearSky}}}{\partial T_S}(x,y)$ is the partial derivative of eq. (11) with respect to surface temperature,
- adopting the fitted parameter values over land and ocean (Table S1).

676

- 677 From our simplified relationships constrained by observed climatology for 2003-2023, the
- annual mean local clear sky albedo feedback (eq. 21: Fig. 7a) reveals high values in the
- Himalayas and high latitude regions where a small temperature change would lead to a large
- variation in clear sky albedo. The zonal mean values evaluated from simplified empirical
- relations and observations here (Fig. 7c, blue) show similarities to the values evaluated for
- 682 CMIP6 models using radiative kernels following a 4xCO₂ perturbation (Fig. 7c, grey), both in
- terms of the maximum magnitude and also the zonal pattern.

- 685 Three key differences arise from the spatially-derived method used here (Fig. 7a, 7c blue)
- compared to the standard temporally-derived radiative kernel method applied to CMIP6
- 687 models (Fig. 7c, grey):

- (1) The method here evaluates the feedback from observations within a reduced physics framework, whereas the radiative kernel method is applied to climate models that contain complex physics but may also contain model bias;
- (2) The method here implicitly considers the cryosphere and water vapor impacts on clear sky albedo, and does not consider any vegetation-induced albedo changes, whereas CMIP6 models with coupled vegetation will include both cryosphere and vegetation induced surface albedo changes but do not consider atmospheric water vapor absorption effects; and
- (3) The method here evaluates $\lambda_{albedo,ClearSky}(x,y)$ for an infinitesimal perturbation to the climate state (eq. 21), whereas the radiative kernel approach applies to a large finite $4xCO_2$ perturbation. Where snow or ice melts early in the large $4xCO_2$ perturbation, this finite approximation will reduce the temporally derived climate feedback relative to an infinitesimal perturbation, since the change in albedo will be the same but the change in the denominator (surface temperature) will be larger.

Anthropogenic forcing is warming future climate beyond an infinitesimal perturbation (IPCC, 2021). To explore large perturbations, our method evaluates $\lambda_{albedo,ClearSky}(x,y)$ for infinitesimal perturbations applied to warmed climate states, using surface temperature patterns for +2K and +4K global mean warming (IPCC, 2021) added on to the 1940-1960 climatological mean in the ERA5 surface temperature record (the earliest period within the ERA5 dataset used). This choice results in reduced $\lambda_{albedo,ClearSky}(x,y)$ for the warmed climate states relative to the 2003-2023 period, especially in northern high latitudes where the cryosphere is in retreat (Figure 7c, compare orange and red to blue). This response explains the higher λ_{albedo} values obtained from our method relative to 4xCO₂ perturbation in CMIP6 models

Uncertainties in $\lambda_{albedo,ClearSky}(x,y)$ are estimated from scaling arguments from the error in $\overline{\alpha_{ClearSky}}(x,y,T_S)$ divided by the range of $\overline{\alpha_{ClearSky}}(x,y,T_S)$: the fractional uncertainty in $\lambda_{albedo,ClearSky}(x,y)$ is estimated as the root mean square error in $\overline{\alpha_{ClearSky}}(x,y,T_S)$ divided by the maximum range of $\overline{\alpha_{ClearSky}}(x,y,T_S)$ over land and ocean (Fig. 5c, blue, red and orange shading).

To calculate the fixed-cloud planetary albedo feedback in all sky conditions, without considering changes in cloud amount or cloud properties,

$$\lambda_{albedo,AllSky} = -R_{in} \frac{\partial \alpha_{AllSky}}{\partial T_S}$$
 (23)

we now calculate $\frac{\partial \alpha_{AllSky}}{\partial T_S}$, by considering the impact of cloudy skies and non-zero cloud amount on $\frac{\partial \alpha_{ClearSky}}{\partial T_S}$ (eq. 22). The partial derivative of cloudy sky albedo is related to the partial derivative of clear sky albedo via differentiating eq. (14) (Supporting Information S1), 728

729
$$\frac{\partial \alpha_{CloudySky}}{\partial T_S} = \left[\frac{[1 - \alpha_{Cloud:dir}(x, y)][1 - \overline{\alpha_{Cloud}}]}{[1 - \overline{\alpha_{Cloud}}]^2 [1 + \beta[0.5 \times [3\sin^2\phi - 1]]]} \right] \frac{\partial \alpha_{ClearSky}}{\partial T_S}$$
(24)

The partial derivatives of albedo with respect to surface temperature in clear sky, all sky and cloudy sky conditions are related, from eq. (7), via,

735
$$\frac{\partial \alpha_{AllSky}}{\partial T_S} = f_{CI} \frac{\partial \alpha_{CloudySky}}{\partial T_S} + [1 - f_{CI}] \frac{\partial \alpha_{ClearSky}}{\partial T_S}$$
 (25)

By substituting (24) and (25) in (17) the fixed-cloud planetary albedo feedback in all sky conditions becomes,

 $\lambda_{albedo,AllSky} = -R_{in} \left[f_{CI} \frac{\left[1 - \overline{\alpha_{Cloud}}\right] \left[1 - \alpha_{Cloud:dir}\right]}{\left[1 - \overline{\alpha_{Cloud}}\right]^{2} \left[1 + \beta \left[0.5 \times \left[3 \sin^{2} \phi - 1\right]\right]\right]} + \left[1 - f_{CI}\right] \right] \frac{\partial \alpha_{ClearSky}}{\partial T_{S}}$ 741 (26)

 The values of $\lambda_{albedo,AllSky}$ are calculated for surface temperatures during the 2003-2023 period (Fig 7b,d), and also for +2K and +4K warmed climate states (Fig. 7d). The $\lambda_{albedo,AllSky}$ for each level of warming is correspondingly reduced relative to $\lambda_{albedo,ClearSky}$, and the $\lambda_{albedo,AllSky}$ values derived here from observations and simplified empirical relations are similar to the CMIP6 derived values using radiative kernels and a 4xCO₂ perturbation (Fig. 7d). Uncertainty in $\lambda_{albedo,AllSky}$ is estimated through the application of the same scaling arguments as adopted for $\lambda_{albedo,ClearSky}$ (Fig. 7c,d, blue, red and orange shading).

The global mean fixed-cloud planetary albedo feedback in all sky conditions is 0.64 (0.58 to 0.70 at 66% confidence) Wm⁻²K⁻¹ for 2003-2023 background surface temperatures, decreasing to 0.54 (0.49 to 0.59) Wm⁻²K⁻¹ if background surface temperatures had already undergone +2K warming (Table 1) and decreasing to 0.35 (0.32 to 0.38) Wm⁻²K⁻¹ for 4K warming. Note that a sensitivity study manually varying the value of β in eq. (10) found that $\lambda_{albedo,AllSky}$ varied by only ±0.05 Wm⁻²K⁻¹ when β varied by ±0.1, which is ten times the uncertainty in β (= 0.33 ± 0.01). Therefore, within uncertainty the value of β does not significantly alter the fixed-cloud albedo within our spatial methodology.

3.3 Water Vapor Lapse Rate feedback

The water vapor-lapse rate (WVLR) feedback is defined here as the change in outgoing longwave radiation per unit warming due to a change in the planetary emissivity of the atmosphere following a change in climate state. From eq. (17) the WVLR feedback for clear skies is,

 $\lambda_{WVLR,ClearSky}(x,y) = -\sigma T_S^4(x,y) \frac{\partial \varepsilon_{ClearSky}}{\partial T_S}(x,y)$ (27)

We now need to evaluate $\frac{\partial \varepsilon_{ClearSky}}{\partial T_S}$ by differentiating the observation-constrained reduced physics relation for $\varepsilon_{ClearSky}$, eq. (13). Assuming that the changes in tropospheric height, midtroposphere relative humidity and surface pressure with a change in climate state alter planetary emissivity significantly less than the change in surface temperature, then the partial derivative becomes,

 $774 \qquad \frac{\partial \varepsilon_{ClearSky}}{\partial T_S} \approx c_1 \tag{28}$

This simplification is a good approximation so long as $\left| \frac{\partial z_{trop}}{\partial T_S} \frac{\partial \varepsilon_{ClearSky}}{\partial z_{trop}} \right|$, $\left| \frac{\partial H_{rel}}{\partial T_S} \frac{\partial \varepsilon_{ClearSky}}{\partial H_{rel}} \right|$ and $\left| \frac{\partial p_S}{\partial T_S} \frac{\partial \varepsilon_{ClearSky}}{\partial p_S} \right|$ are each much smaller than $\left| \frac{\partial \varepsilon_{ClearSky}}{\partial T_S} \right|$, (eq. 6), reflecting how the changes in tropospheric height, mid-troposphere relative humidity and surface pressure with a change in climate state alter planetary emissivity significantly less than the change in surface temperature.

Substituting (28) into (27), and using the constrained value of $c_1 = \frac{\partial \varepsilon_{ClearSky}}{\partial T_S} =$ $-(2.904 \pm 0.003) \times 10^{-3} \text{ K}^{-1}, \text{ gives } \lambda_{WVLR,ClearSky} \text{ varying from approximately 0.5 Wm}^{-2}\text{K}^{-1} \text{ in cold regions to 1.5 Wm}^{-2}\text{K}^{-1} \text{ in warm regions (Fig. 8, left hand column).}$

Uncertainty in the value of $\lambda_{WVLR,ClearSky}$ is due to our assumption that $\varepsilon_{ClearSky}$ is related to T_S via a linear term in eq. (13), c_1T_S . The observed relation between spatial variation in $\varepsilon_{ClearSky}$ and T_S in modern climatology does reveal an approximate linear relation (Fig. 4e), which informs the decision to assume a linear term in eq. (13) as a best estimate for the functional relationship. However, a non-linear relationship is still possible. Supporting Information S2 evaluates the uncertainty in $\lambda_{WVLR,ClearSky}$ that arises from the introduction of a non-linear term between $\varepsilon_{ClearSky}$ and T_S via modification of eq. (13), whereby the c_1T_S term becomes $c_1T_S^n$. The systematic uncertainty in $\lambda_{WVLR,ClearSky}$ arising from the linear assumption is evaluated in assuming that the value of the power varies with a normal distribution with mean 1 and standard deviation 1, $n{\sim}N(1,1)$ (Supporting Information S2; Fig. 8c, blue shading). The relatively small systematic uncertainty introduced by the linear assumption (Fig. 8c), combined with the good statistical fit for eq. (13) (Figure 2; Table S2), provides confidence in the evaluation of $\lambda_{WVLR,ClearSky}$ (Fig. 8a,c)

The WVLR feedback in all sky conditions is given by,

802
$$\lambda_{WVLR,AllSky}(x,y) = -\sigma T_S^4(x,y) \frac{\partial \varepsilon_{AllSky}}{\partial T_S}(x,y)$$
 (29)

where it is assumed that both cloud amount, f_{CA} , and cloud type are unchanging with perturbation. The impact on outgoing longwave radiation of cloud type is represented in this study by the cloud-emissivity coefficient, c_{ε} (eq. 16; Goodwin and Williams, 2023) in eq. (15),

relating ε_{AllSky} to $\varepsilon_{ClearSky}$, f_{CA} and c_{ε} . Therefore, to identify $\frac{\partial \varepsilon_{AllSky}}{\partial T_S}(x,y)$ as a function of $\frac{\partial \varepsilon_{ClearSky}}{\partial T_S}(x,y)$, we differentiate eq. (15) with respect to surface temperature holding f_{CA} and

 c_{ε} constant to reveal,

811
$$\frac{\partial \varepsilon_{AllSky}}{\partial T_S}(x,y) = \left[1 - f_{CA}(x,y) + f_{CA}(x,y)c_{\varepsilon}(x,y)\right] \frac{\partial \varepsilon_{ClearSky}}{\partial T_S}(x,y) \tag{30}$$

Substituting (30) into (29) then reveals the WVLR feedback in all sky conditions in terms of the sensitivity of clear sky planetary emissivity to surface temperature, the cloud amount area fraction, the cloud-emissivity coefficient, surface temperature and the Stefan-Boltzmann constant,

$$\lambda_{WVLR,AllSky}(x,y) = -\sigma T_S^4 [1 - f_{CA} + f_{CA}c_{\varepsilon}] \frac{\partial \varepsilon_{ClearSky}}{\partial T_S}(x,y)$$
(31)

This relation is evaluated for the observed climatology from 2003-2023, revealing $\lambda_{WVLR,AllSky}$ spatially (Fig. 8b) and for zonal averages (Fig. 8d), where zonal averages include the systematic uncertainty from the assumption of a linear term relating $\varepsilon_{ClearSky}$ and T_S (Fig. 8d, blue shading; Supporting Information S2). The magnitudes of zonal average $\lambda_{WVLR,AllSky}$ are generally similar to CMIP6 model values approximated through radiative kernels and a 4xCO₂ temporal perturbation (Fig. 8d), but show a smoother latitudinal variation. This may reflect a difference between how cloud amount and type are held constant between the methodologies ($\delta c_{\varepsilon} = 0$ and $\delta f_{CA} = 0$ here versus imposed constant simulated cloud amount and type in the CMIP6 simulations). These different methodologies may then imply differences in how clouds interact with non-cloud features of the air column that are changing with perturbation (e.g. water vapor content, aerosols) to affect longwave radiation.

The global mean all sky WVLR feedback is 1.28 (1.13 to 1.45) Wm⁻²K⁻¹ for the 2003-2023 surface temperatures (Table 1). Our analysis suggests that the WVLR feedback only increases a small amount as the world warms, although we note that we do not have a strong constraint on the second derivative of planetary emissivity with surface temperature from our observationally constrained functional relationship (eq. 13, Supporting Information S2). Therefore, we have low confidence in the WVLR feedback evaluation for the +2 K and +4 K warmed worlds. When comparing to other studies, note that our methodology includes only the LW component of the WVLR feedback (Table 1), the SW component arising from changes in water vapor absorbing or scattering SW radiation is implicitly included within our clear sky and fixed-cloud planetary albedo feedbacks. Note also the similarity between our estimate and temporally derived estimates arises even though not all processes that act temporally may be included within the spatial analysis used to constrain WVLR here (see section 2.2.2 above).

3.4 Global mean total feedback

847 The global mean values of the Planck, WVLR and fixed-cloud planetary albedo feedbacks are analyzed from spatial variation for the 2003-2023 climatology combined with a +2K warming 848 849 pattern (Table 1), and are similar in magnitude to values analyzed using temporal perturbation methods (IPCC, 2021; Sherwood et al., 2020; Zelinka et al, 2020). While the Planck and WVLR 850 feedbacks are consistent (Table 1), the fixed-cloud planetary albedo feedback for the 2003-851 2023 climatology is larger than recent estimates for surface albedo from temporal variation by 852 around 0.3 Wm⁻²K⁻¹. Two possible reasons for this include: Firstly, our fixed-cloud planetary 853 albedo estimate implicitly includes both how surface albedo changes with temperature from 854 855 the cryosphere and how atmospheric albedo changes with temperature from water vapor-lapse rate effects. These shortwave water vapor-lapse rate effects are not included within estimates 856 of surface albedo (IPCC, 2021; Sherwood et al., 2020; Zelinka et al., 2020) but are estimated at 857 around 0.3 Wm⁻²K⁻¹ (Donohoe et al., 2014). Note this also implies that our WVLR feedback is 858 859 actually more consistent with the Sherwood et al. (2020) estimate, since we do not include the 860 shortwave component (Table 1). Secondly, our fixed-cloud albedo estimate is calculated for an 861 infinitesimal perturbation to the 2003-2023 climatology, whereas previous surface albedo estimates are calculated for a large 4xCO2 perturbation. Our albedo estimate becomes more 862 consistent with previous estimates when the world has warmed by +2K and +4K above the mid-863 20th century average. 864

865

866 867

868

869 870

871872

873874

875

876

877

878

879

880

881 882

883

884 885

886 887

888

889

To calculate total climate feedback, $\lambda_{total} = \Sigma \lambda_X$, we combine our Planck, WVLR and fixedcloud planetary -albedo feedback estimates in all sky conditions with two estimates of cloud feedback: Ceppi and Nowack (2021): $\lambda_{cloud} = 0.43 \pm 0.35 \text{ Wm}^{-2}\text{K}^{-1}$ at 90% confidence that applies after a 4xCO₂ perturbation after surface warming patterns have adjusted; and Raghuraman et al., (2023) $\lambda_{cloud} = 0.20 \pm 0.34 \, \text{Wm}^{-2} \text{K}^{-1}$ at 95% confidence that applies in the present climate state before any future adjustments to surface warming patterns. Note that these cloud feedback estimates are similar to estimates from recent reviews of the literature (IPCC, 2021; Sherwood et al., 2020; Table 1), with Ceppi and Nowack (2021) toward the more amplifying range and Raghuraman et al., (2023) toward the less amplifying range. We calculate the total global mean climate feedback only for the 2003-2023 climatology, since we have low confidence in the WVLR feedbacks for the +2 and +4 K warmed worlds (Table 1). Assuming independent uncertainty between terms, our analysis combined with Ceppi and Nowack (2021) provides a $\lambda_{total} = -0.95$ [-0.49 to -1.40 at 90% confidence] Wm⁻²K⁻¹ for the 2003-2023 period (Table 1; Fig. 8a), while when combined with Raghuraman et al., (2023) we find $\lambda_{total} =$ -1.18 [-0.77 to -1.58] Wm²K⁻¹. Our spatially-derived estimates are consistent with previous temporal variation methods for calculating total climate feedback (Figure 9; Table 1: IPCC, 2021; Sherwood et al., 2020; Zelinka et al., 2020), with the choice of cloud feedback determining whether our best estimate is more similar to the mean of the CMIP6 models or the IPCC (2021) AR6 (Table 1), although noting that the Ceppi and Nowack (2021) cloud feedback estimate applies after a 4xCO₂ perturbation and so is more directly relevant as a comparison to the previous net climate feedback estimates (Table 1). Note that in the Sherwood et al. (2020) review, additional evidence is used to constrain Equilibrium Climate Sensitivity (ECS) that is not used to constrain the climate feedback, and therefore the reduced range of our λ_{total} estimate relative to Sherwood et al (2020) (Figure 9) does not imply a similarly reduced range for ECS.

4. Discussion

Many existing methods evaluate climate feedbacks from the *temporal* variation in climate state following some perturbation (e.g. Sherwood et al., 2020). When applied to numerical climate models, the temporal variation is induced by application of finite perturbations to the climate system, often with a quadrupling of atmospheric CO₂ (e.g. Soden et al., 2008; Zelinka et al. 2020). Observation-based methods (e.g. Cael et al., 2023; Sherwood et al., 2020; Goodwin, 2021; Goodwin and Cael, 2021) often employ the recent temporal changes in surface temperature and outgoing radiation at the top of the atmosphere, where time-mean net outgoing radiation is sometimes deduced from heat content changes in the ocean and Earth system. Paleoclimate approaches avoid the need to calculate Earth's transient energy imbalance by considering longer timescales, but do rely on proxy evidence to reconstruct the observable quantities (e.g. Rohling et al., 2018). Other approaches involving observational records include using the internal variability within observational records to constrain climate feedback (Dessler, 2013) and applying emergent constraints to assess which complex climate models have the best simulated representation of the climate's sensitivity to change (e.g. Cox et al., 2018).

This study has presented a new methodology for evaluating climate feedbacks, where simplified relations between outgoing radiation and climatological properties (eqns. 1-30) are empirically constrained with *spatial* variation in observed climatology (Hersbach et al., 2023; Loeb et al., 2018; Figs. 1-6), and then differentiated with respect to surface temperature to reveal the Planck, WVLR and fixed-cloud planetary albedo feedbacks (Figs. 7, 8). The climate feedbacks are evaluated spatially at 1° by 1° horizontal resolution, and then a global mean is found by convoluting with a spatial warming pattern.

When spatial variation is considered, both TOA outgoing longwave radiation and outgoing shortwave radiation vary considerably with surface temperature (e.g. Fig. 2c,d for clear skies), which is expressed via spatial variation in planetary emissivity and planetary albedo respectively (Fig. 2e,f). Our simplified and empirically constrained relations identify that 91% of the apparent spatial link between clear sky albedo and surface temperature arises through a functional dependance. The remaining 9% of the apparent spatial link arises through the latitudinal effect on the solar-zenith angle, which co-varies with surface temperature in space but would not co-vary with temperature in time following perturbation. Similarly, we identify that around 77% of the apparent spatial link between clear sky planetary emissivity and surface temperature arises through a functional dependence. The remaining 23% of this apparent spatial link arises through factors that co-vary with surface temperature in space but would not co-vary in time following perturbation, such as surface pressure and the height of the tropopause. Through extracting these co-varying factors, our methodology uses observed spatial variation in outgoing radiation and surface temperature to evaluate climate feedbacks following perturbation.

Our spatial-variation methodology is complementary to existing temporal-variation methods, with consistent results (Table 1) derived from independent evidence, assumptions and uncertainties. For example, the reduced physics nature of our approach contrasts with the

complex climate models used for evaluating climate feedbacks in the literature (e.g. Zelinka et al., 2020). However, the ability to evaluate climate feedbacks from spatial variation in observed climatology produces a significantly better signal-to-noise ratio (with spatial temperatures and outgoing radiation varying by order 80 K and 100 Wm⁻²K⁻¹ respectively) when compared to historic observations of temporal changes in temperature and outgoing radiation (of order 1 K and 1 Wm⁻²K⁻¹ respectively). When producing an estimate of climate feedback, and the related Equilibrium Climate Sensitivity, from multiple lines of evidence using a Bayesian framework then a method that is largely independent of pre-existing methods can be useful in narrowing the overall uncertainty range (Sherwood et al., 2020), such as the method presented here (e.g. Fig. 9).

Our best estimate for global mean total climate feedback analyzed from spatial information, comes out similar in magnitude to the IPCC (2021) AR6 and Sherwood et al. (2020) estimates, depending on the independent cloud feedback estimate used (Table 1). One difference in methodology is that our spatial estimate considers the albedo feedback for an infinitesimal warming perturbation, whereas the IPCC (2021) and Sherwood et al. (2020) estimates consider a 4xCO₂ perturbation with relatively large finite warming. When we apply our methodology to calculate the albedo feedback for infinitesimal perturbation starting from a warmed world (Table 1; Fig. 7), there is a reduction in the positive albedo feedback by a magnitude enough to explain the difference between our estimate of total climate feedback and the IPCC (2021) and Sherwood et al (2020) estimates.

Acknowledgments

The authors declare no financial conflicts of interest.

Open Research

The ERA5 reanalysis (Hersbach et al., 2023) for monthly averaged data on single levels is available for download here: https://doi.org/10.24381/cds.f17050d7 (accessed 31-03-2024). The CERES Energy Balanced and filled (EBAF4.2) satellite observation dataset used here for the period 2003-2023 (Loeb et al., 2018) is available here: https://doi.org/10.5067/TERRA-AQUA-NOAA20/CERES/EBAF-TOA_L3B004.2 (accessed 08/04/2024; dataset reference: NASA/LARC/SD/ASDC (2022)). CMIP data were obtained from the UK Centre for Environmental Data Analysis portal (https://esgf-index1.ceda.ac.uk/search/cmip6-ceda/; dataset reference WCRP (2024)). We acknowledge the WCRP, which, through its Working Group on Coupled Modeling, coordinated and promoted CMIP6. We thank the climate-modeling groups for producing and

making available their model output, the Earth System Grid Federation (ESGF) for archiving the data and
providing access and the multiple funding agencies that support CMIP6 and ESGF. Code for calculating the
height of the tropopause, from Mateus et al. (2022), is available for download here:
https://github.com/pjmateus/global_tropopause_model (accessed 14/04/2023, Model code reference
Mateus et al. (2022b)); where this study uses the options for a bilinear interpolation model of the
tropopause, and a surface at 3.0 potential vorticity units, where 1 potential vorticity unit is equal to $10^{-6}~\rm K~kg^{-1}$
m ² s ⁻¹ . The GMTED2010 dataset for mean surface elevation (Danielson & Gesch, 2011) is available here:
https://temis.nl/data/gmted2010/ (accessed 18/03/2024; Dataset reference USGS (2011)). The matlab code
developed here for conducting the analysis here is available at https://github.com/WASP-
ESM/Spatial Climate Feedback/tree/main (model code reference Goodwin et al. (2025)
https://doi.org/10.5281/zenodo.15624497). Note that the code requires separate download of datasets
mentioned above.
References
References Cael, B. B., Bloch-Jonhson, J., Ceppi, P., Fredriksen, HB., Goodwin, P., Gregory, J.M., Smith, C.J.
Cael, B. B., Bloch-Jonhson, J., Ceppi, P., Fredriksen, HB., Goodwin, P., Gregory, J.M., Smith, C.J.
Cael, B. B., Bloch-Jonhson, J., Ceppi, P., Fredriksen, HB., Goodwin, P., Gregory, J.M., Smith, C.J. & Williams, R.G. (2023), Energy budget diagnosis of changing climate feedback. <i>Science</i>
Cael, B. B., Bloch-Jonhson, J., Ceppi, P., Fredriksen, HB., Goodwin, P., Gregory, J.M., Smith, C.J. & Williams, R.G. (2023), Energy budget diagnosis of changing climate feedback. <i>Science</i>
Cael, B. B., Bloch-Jonhson, J., Ceppi, P., Fredriksen, HB., Goodwin, P., Gregory, J.M., Smith, C.J. & Williams, R.G. (2023), Energy budget diagnosis of changing climate feedback. <i>Science Advances</i> 9, 16, eadf9302, doi:10.1126/sciadv.adf9302.
Cael, B. B., Bloch-Jonhson, J., Ceppi, P., Fredriksen, HB., Goodwin, P., Gregory, J.M., Smith, C.J. & Williams, R.G. (2023), Energy budget diagnosis of changing climate feedback. <i>Science Advances</i> 9, 16, eadf9302, doi:10.1126/sciadv.adf9302. Ceppi, P., and Nowack, P. (2021) Observational evidence that cloud feedback amplifies global

991	Cox, P., Huntingford, C. and Williamson, M. (2018) Emergent constraint on equilibrium climate
992	sensitivity from global temperature variability, <i>Nature</i> 553, 319–322, doi:10.1038/nature25450.
993	
994	Cronin, T. W. (2014). On the choice of average solar zenith angle. Journal of the Atmospheric
995	Sciences, 71(8), 2994-3003. https://doi.org/10.1175/JAS-D-13-0392.1
996	
997	Danielson, J.J., & Gesch, D.B. (2011), Global multi-resolution terrain elevation data 2010
998	(GMTED2010): U.S. Geological Survey Open-File Report 2011–1073, 26 p.
999	
1000	Dessler, A. E. (2013), Observations of Climate Feedbacks over 2000–10 and Comparisons to
1001	Climate Models, Journal of Climate, 26, 333–342, doi:10.1175/JCLI-D-11-00640.1.
1002	
1003	Donohoe, A., Armour, K.C., Pendergrass, A.G., & Battisti, D.S. (2014) Shortwave and longwave
1004	radiative contributions to global warming under increasing CO2, Proc. Natl. Acad. Sci. U.S.A. 111
1005	(47) 16700-16705, https://doi.org/10.1073/pnas.1412190111
1006	
1007	Feng, J., Paynter, D., & Menzel, R. (2023). How a stable greenhouse effect on Earth is
1008	maintained under global warming. Journal of Geophysical Research: Atmospheres, 128(9),
1009	e2022JD038124.
1010	

1011	Feng, J., Paynter, D., Wang, C., & Menzel, R. (2023). How atmospheric humidity drives the
1012	outgoing longwave radiation-surface temperature relationship and inter-model spread.
1013	Environmental Research Letters, 18(10), 104033.
1014	
1015	Goodwin, P. (2021), Probabilistic projections of future warming and climate sensitivity
1016	trajectories, Oxford Open Climate Change, 1, 1, kgab007,
1017	https://doi.org/10.1093/oxfclm/kgab007
1018	
1019	Goodwin, P. & Cael, B.B. (2021), Bayesian estimation of Earth's climate sensitivity and transient
1020	climate response from observational warming and heat content datasets. Earth System
1021	Dynamics, 12, 709–723, doi:10.5194/esd-12-709-2021.
1022	
1023	Goodwin, P. & Williams, R.G. (2023) On the Arctic Amplification of surface warming in a
1024	conceptual climate model, <i>Physica D: Nonlinear Phenomena</i> , doi:10.1016/j.physd.2023.133880
1025	
1026	Goodwin, P., Williams, R.G., Ceppi, P. and Cael., B.B. (2025) Spatial climate feedbacks derived
1027	from spatial gradients in recent climatology model code [model code]
1028	https://doi.org/10.5281/zenodo.15624497
1029	
1030	Gregory, J. M., & Andrews, T. (2016). Variation in climate sensitivity and feedback parameters
1031	during the historical period. Geophysical Research Letters, 43(8), 3911-3920.
1032	https://doi.org/10.1002/2016GL068406

1033	
1034	Hartmann, D.L. (1994), Global Physical Climatology, Academic Press, San Diego, USA. ISBN 0-12-
1035	328530-5. 411 pp.
1036	
1037	Hersbach, H., Muñoz Sabater, J., Nicolas, Rozum, I., Simmons, Vamborg, F., A., Bell, B.,
1038	Berrisford, P., Biavati, G., Buontempo, C., Horányi, A., J., Peubey, C., Radu, R., Schepers, D., Soci
1039	C., Dee, D. & Thépaut, J-N. (2018), Essential climate variables for assessment of climate
1040	variability from 1979 to present, Copernicus Climate Change Service (C3S) Data Store (CDS),
1041	(Accessed on 31-03-2024) [Dataset] https://doi.org/10.24381/cds.f17050d7
1042	
1043	Ingram, W. (2010) A very simple model for the water vapour feedback on climate change. Q. J.
1044	R. Meteorol. Soc. 136, 646, 30-40. https://doi.org/10.1002/qj.546.
1045	
1046	IPCC (2021), Climate Change 2021: The Physical Science Basis. Contribution of Working Group I
1047	to the Sixth Assessment Report of the Intergovernmental Panel on Climate Change [Masson-
1048	Delmotte, V., Zhai P., Pirani, A., Connors, S.L., Péan, C., Berger, S., Caud, N., Chen, Y., Goldfarb,
1049	L., Gomis, M.I., Huang, M., Leitzell, K., Lonnoy, E., Matthews, J.B.R., Maycock, T.K., Waterfield,
1050	T., Yelekçi, O., Yu, R., and Zhou, B. (eds.)]. Cambridge University Press, Cambridge, United
1051	Kingdom and New York, NY, USA, doi: 10.1017/9781009157896.
1052	

1053	Koll, D.D.B., and Cronin, T.W. (2018) Earth's outgoing longwave radiation linear due to H ₂ O
1054	greenhouse effect. Proc. Natl. Acad. Sci. U.S.A. 115 (41) 10293-10298.
1055	https://doi.org/10.1073/pnas.1809868115.
1056	
1057	Koll, D. D., Jeevanjee, N., and Lutsko, N. J. (2023). An analytic model for the clear-sky longwave
1058	feedback. Journal of the Atmospheric Sciences, 80(8), 1923-1951. https://doi.org/10.1175/JAS
1059	<u>D-22-0178.1</u>
1060	
1061	Loeb, N.G., Doelling, D.R., Wang, H., Su, W., Nguyen, C., Corbett, J.G., Liang, L., Mitrescu, C.,
1062	Rose, F.G. and Kato, S. (2018), Clouds and the earth's radiant energy system (CERES) energy
1063	balanced and filled (EBAF) top-of-atmosphere (TOA) edition-4.0 data product. Journal of
1064	Climate, 31(2), 895-918, doi:10.1175/JCLI-D-17-0208.1.
1065	
1066	Mateus, P., Mendes, V.B. and Pires, C.A.L. (2022), Global Empirical Models for Tropopause
1067	Height Determination, Remote Sensing 14, 4303, doi:10.3390/rs14174303.
1068	
1069	Mateus, P., Mendes, V.B. and Pires, C.A.L. (2022b), Global Tropopause Models [model code].
1070	Accessed via https://github.com/pjmateus/global tropopause model (associated with
1071	doi:10.3390/rs14174303)
1072	

1073	NASA/LARC/SD/ASDC. (2022). CERES Energy Balanced and Filled (EBAF) TOA Monthly means
1074	data in netCDF Edition4.2 [Dataset]. NASA Langley Atmospheric Science Data Center DAAC.
1075	Retrieved from https://doi.org/10.5067/TERRA-AQUA-NOAA20/CERES/EBAF-TOA L3B004.2
1076	
1077	Payne, R.E. (1972) Albedo of the Sea Surface. Journal of the Atmospheric Sciences, 25, 5, 959-
1078	970. doi:10.1175/1520-0469(1972)029<0959:AOTSS>2.0.CO;2
1079	
1080	Pincus, R., et al. (2015), Radiative flux and forcing parameterization error in aerosol-free clear
1081	skies, Geophys. Res. Lett., 42, 5485–5492, doi:10.1002/2015GL064291.
1082	
1083	Raghuraman, S. P., Paynter, D., Menzel, R., & Ramaswamy, V. (2023). Forcing, cloud feedbacks,
1084	cloud masking, and internal variability in the cloud radiative effect satellite record. Journal of
1085	Climate, 36(12), 4151-4167. https://doi.org/10.1175/JCLI-D-22-0555.1
1086	
1087	Raval, A., Ramanathan, V. (1989) Observational determination of the greenhouse
1088	effect. Nature 342, 758–761. https://doi.org/10.1038/342758a0
1089	
1090	Roemer, F. E., Buehler, S. A., Brath, M., Kluft, L., & John, V. O. (2023). Direct observation of
1091	Earth's spectral long-wave feedback parameter. <i>Nat. Geosci.</i> 16, 416–421.
1092	https://doi.org/10.1038/s41561-023-01175-6
1093	

1094	Schmidt, G.A., Ruedy, R., Miller, R.L., and Lacis, A.A. (2010) Attribution of the present-day total
1095	greenhouse effect. J. Geophys. Res., 115, D20106, https://doi.org/10.1029/2010JD014287
1096	
1097	Sherwood, S. C., Webb, M. J., Annan, J. D., Armour, K. C., Forster, P. M., Hargreaves, J. C.,
1098	Hegerl, G., Klein, S. A., Marvel, K. D., Rohling, E. J., Watanabe, M., Andrews, T., Braconnot,
1099	P., Bretherton, C. S., Foster, G. L., Hausfather, Z., von der Heydt, A. S., Knutti, R., Mauritsen,
1100	T., Norris, J. R., Proistosescu, C., Rugenstein, M., Schmidt, G. A., Tokarska, K. B. & Zelinka, M.
1101	D. (2020). An assessment of Earth's climate sensitivity using multiple lines of evidence. Reviews
1102	of Geophysics, 58, e2019RG000678. https://doi.org/10.1029/2019RG000678
1103	
1104	Soden, B. J., Held, I.M., Colman, R., Shell, K.M., Kiehl, J. T. & Shields, C. A. (2008), Quantifying
1105	Climate Feedbacks Using Radiative Kernels, Journal of Climate, 21, 3504–3520,
1106	doi:10.1175/2007JCLI2110.1.
1107	
1108	Stephens, G.L. (1978), Radiation Profiles in Extended Water Clouds. II: Parameterization
1109	Schemes. Journal of Atmospheric Sciences 35, 2123-2132, doi:10.1175/1520-
1110	0469(1978)035<2123:RPIEWC>2.0.CO;2.
1111	
1112	Taylor, K. E., Crucifix, M., Braconnot, P., Hewitt, C. D., Doutriaux, C., Broccoli, A. J., Mitchell, J. F.
1113	B. and M. J. Webb (2007), Estimating Shortwave Radiative Forcing and Response in Climate
1114	Models, Journal of Climate, 20, 2530–2543, doi:10.1175/JCLI4143.1.
1115	

1116	USGS (2011) GMTED2010 global digital elevation model (accessed 18/03/2024) [Dataset].
1117	Available https://temis.nl/data/gmted2010/
1118	
1119	WCRP (2024) Coupled Model Intercomparison Project (Phase 6) [Dataset] (Accessed
1120	08/04/2024) https://esgf-index1.ceda.ac.uk/search/cmip6-ceda/
1121	
1122	Zelinka, M. D., Myers, T. A., McCoy, D. T., Po-Chedley, S., Caldwell, P. M., Ceppi, P., Klein, S. A. &
1123	Taylor, K. E. (2020), Causes of higher climate sensitivity in CMIP6 models, Geophysical Research
1124	Letters, 47, e2019GL085782, doi:10.1029/2019GL085782.

1125 Figures and captions:

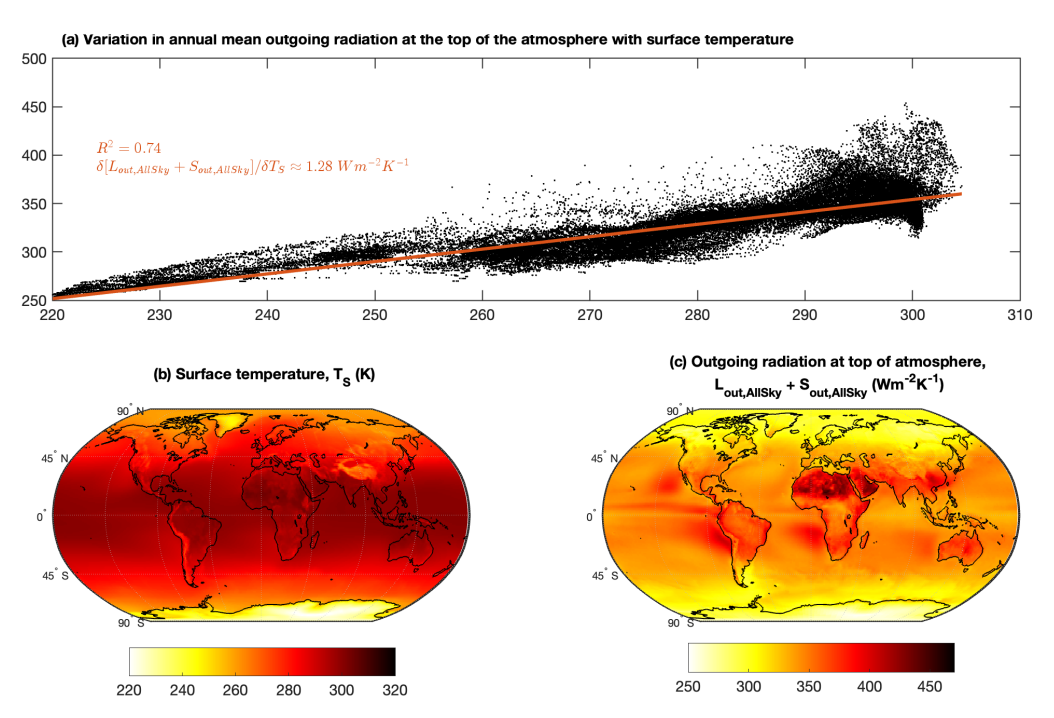


Figure 1. Spatial variation in total outgoing radiation correlating with surface temperature for the 2003-2023 period, analyzed as annual-mean climatology, with each dot (a) representing a single location with 1 deg by 1 deg horizontal resolution. Surface temperature (b) evaluated from ERA5 (Hersbach et al., 2023) and outgoing radiation (c) from EBAF4.2 (Loeb et al., 2018).

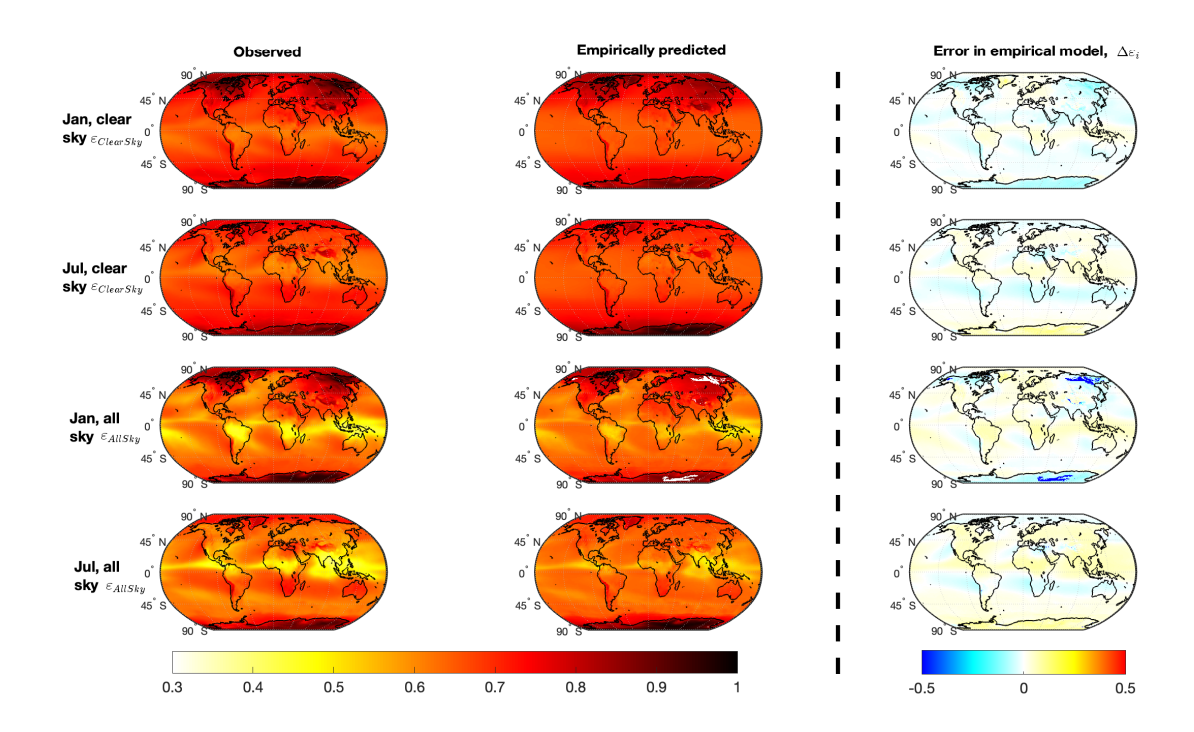


Figure 2: Monthly climatological planetary emissivity for 2003-2023 from observations (left hand column), a reduced physics simplified empirical relation (middle column) and the error in the empirical relation (right hand column). Shown are planetary emissivity in clear sky conditions (top two rows) and all sky conditions (bottom two rows) for the months of January and July.

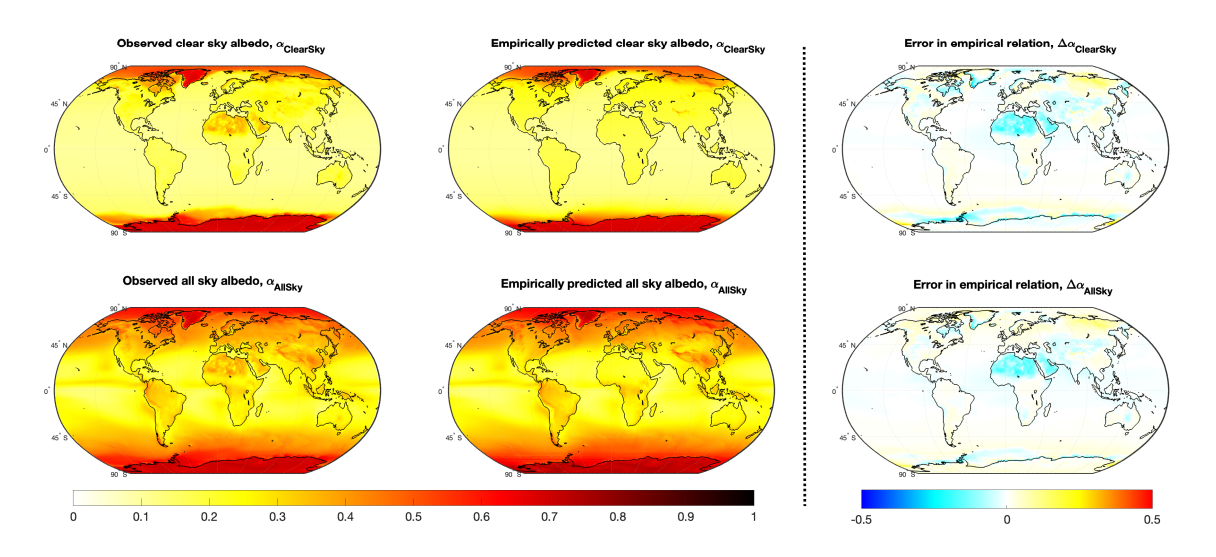


Figure 3: Annual climatological albedo in all sky and clear sky conditions from observations (left hand column), from the empirically constrained predictions (middle column) and the error in the empirical predictions (right hand column). The rms error in the empirical relation for planetary albedo is 0.037 for clear sky and 0.030 for all sky conditions.

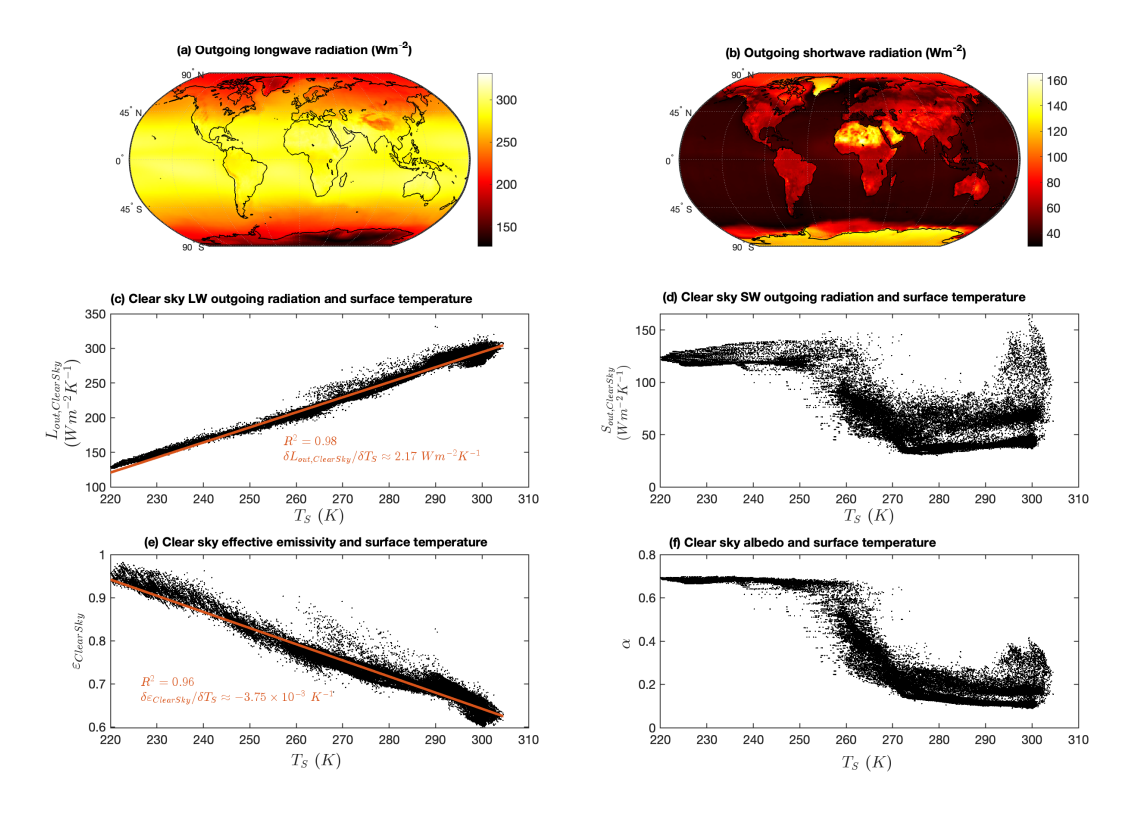
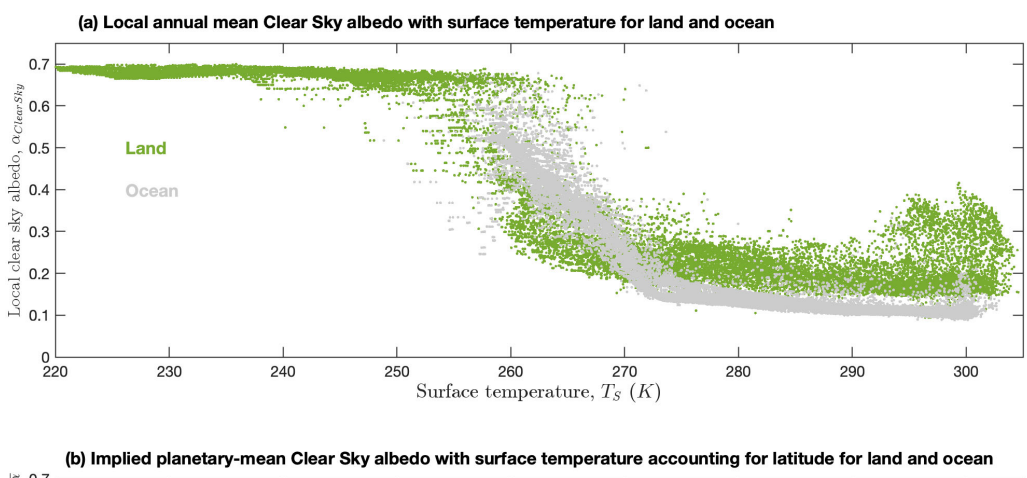


Figure 4. Spatial variation in outgoing radiation, planetary emissivity and albedo for the 2003-2023 period in clear sky conditions, analyzed as annual-mean climatology for 1° by 1° horizontal resolution. (a) Outgoing longwave radiation in clear sky conditions. (b) Outgoing shortwave radiation in clear sky conditions and surface temperature. (d) Outgoing shortwave radiation in clear sky conditions and surface temperature. (e) Planetary emissivity in clear sky conditions and surface temperature. (f) Planetary albedo in clear sky conditions and surface temperature.



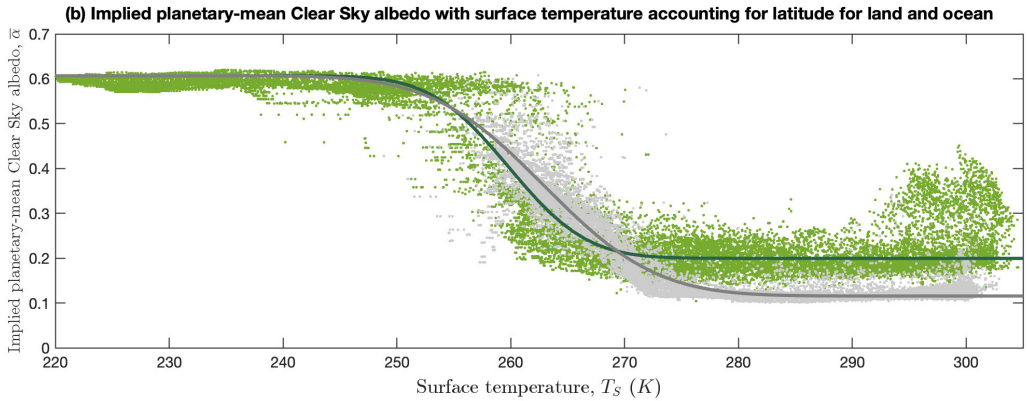


Figure 5. Local albedo over land and ocean with surface temperature for the climatological period 2003-2023. (a) The local annual-mean clear sky planetary albedo with surface temperature evaluated over 1° by 1° resolution. (b) The implied global-mean clear sky planetary albedo if the entire planet was covered in the surface-type found at that location, evaluated over 1° by 1° resolution.

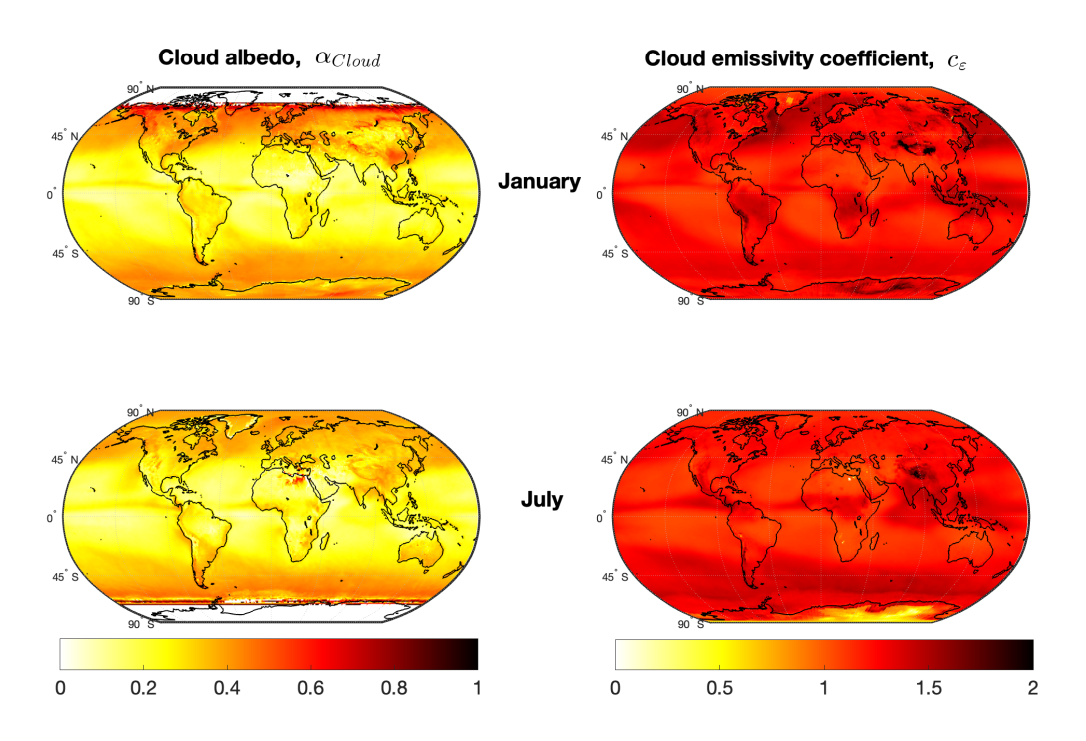


Figure 6. The albedo of cloud for directed incident solar radiation (left hand panels) and the cloud emissivity coefficient for outgoing longwave radiation (right hand panels) and the albedo of cloud from monthly mean climatology for 2003-2023.

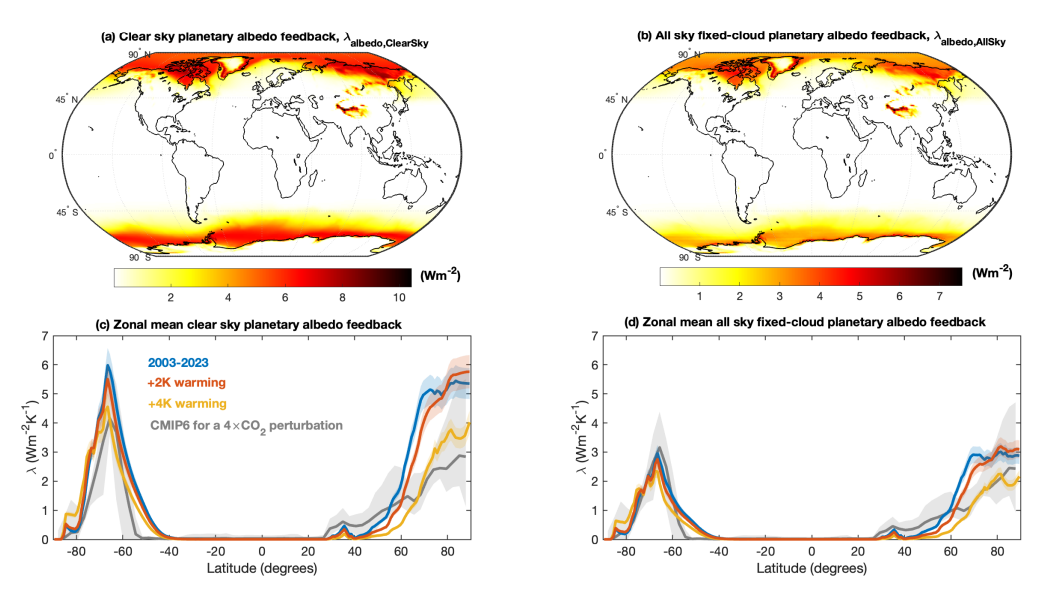


Figure 7. Clear sky and fixed-cloud planetary albedo feedback spatially and as a zonal average. The spatial planetary albedo feedback for the 2003-2023 period for (a) clear sky and (b) fixed-cloud all sky conditions. The zonal mean planetary albedo feedback for (c) clear sky and (d) fixed-cloud all sky conditions. Zonal mean feedbacks shown are for infinitesimal perturbation starting from the 2003-2023 climatology (blue), starting from a 2K warmed climate state (red) and starting from a 4K warmed climate state (orange). Zonal mean surface albedo feedback for finite 4xCO₂ perturbation is shown for CMIP6 models (grey), evaluated from radiative kernels, for comparison.

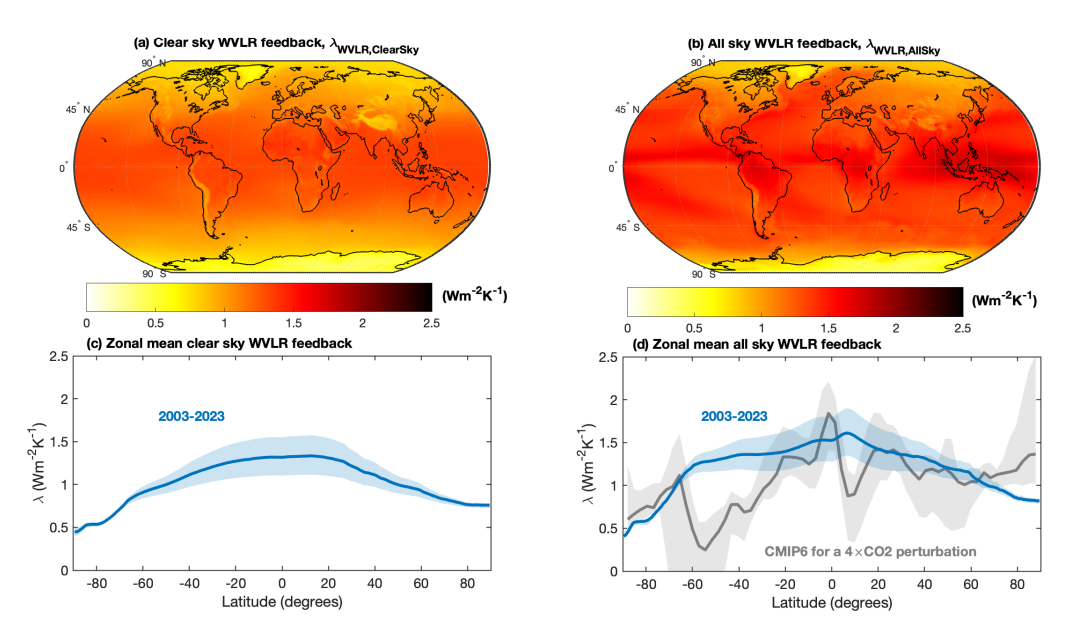


Figure 8. The WVLR feedback spatially and as a zonal average for clear sky and all sky conditions. The spatial WVLR feedback for the 2003-2023 period for (a) clear sky and (b) all sky conditions. The zonal mean WVLR feedback for (c) clear sky and (d) all sky conditions. Zonal mean feedbacks shown are for infinitesimal perturbation starting from the 2003-2023 climatology (blue) and for finite $4xCO_2$ perturbation for CMIP6 models (grey), evaluated from radiative kernels.

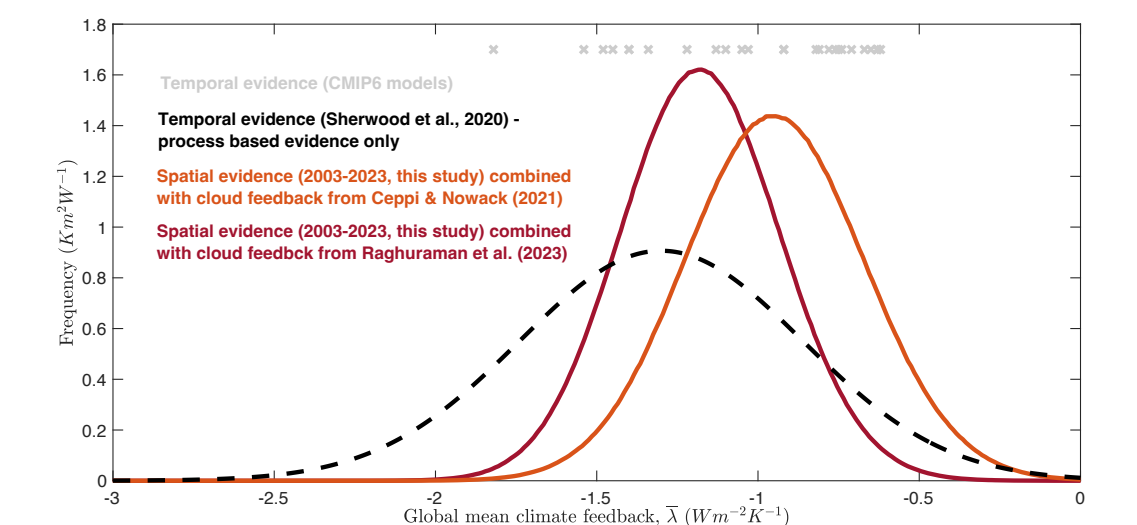


Figure 9. Frequency distributions for effective global mean climate feedback, and values for individual CMIP6 models. Shown are constraints from spatial evidence from this study (blue line), and externally calculated temporal evidence values including for CMIP6 models (gray crosses: Zelinka et al., 2020), and from a recent review (black dashed line: Sherwood et al., 2020).

Table and Table caption:

Climate feedback	This study, 2003-2023 {median, (66% range) [90% range]}	This study, +2°C warming {median, (66% range) [90% range]}	This study, +4°C warming {median, (66% range) [90% range]}	AR6 {median, (66% range) [90% range]}	Sherwood et al. {median, (66% range) [90% range]}	CMIP6, {mean ± standard deviation}
Planck, λ _{Planck} (Wm ⁻² K ⁻¹)	-3.30	-3.38	-3.52	-3.22 (-3.1 to -3.3) [-3.0 to -3.4]	-3.20 (-3.16 to -3.24) [-3.13 to -3.27]	-3.28±0.05
Fixed-cloud albedo, λ_{albedo} (Wm $^{ ext{-}2}$ K $^{ ext{-}1}$)	0.64 (0.58 to 0.70) [0.53 to 0.74]	0.54 (0.49 to 0.59) [0.44 to 0.63]	0.35 (0.32 to 0.38) [0.29 to 0.41]	0.35 (0.25 to 0.45) [0.10 to 0.60]	0.30 (0.15 to 0.45) [0.05 to 0.55]	0.45±0.09
WVLR, λ _{WVLR} (Wm ⁻² K ⁻¹)	1.28 (1.13 to 1.45) [1.02 to 1.57]	1.30° (1.14 to 1.47) [1.03 to 1.60]	1.35 ^a (1.17 to 1.53) [1.05 to 1.67]	1.30 (1.2 to 1.4) [1.1 to 1.5]	1.15 (1.0 to 1.3) [0.9 to 1.4]	1.33±0.09
Cloud, λ_{Cloud} (Wm ⁻² K ⁻¹)	-	-	-	0.42 (0.12 to 0.72) [-0.10 to 0.94]	0.45 (0.12 to 0.78) [-0.09 to 0.99]	0.42±0.36
Total climate feedback, λ_{total} (Wm $^{ ext{-}2}$ K $^{ ext{-}1}$)	-0.95 ^b (-0.68 to -1.21) [-0.49 to -1.40] -1.18 ^c (-0.94 to -1.41) [-0.77 to -1.58]	-	-	-1.16 (-0.78 to -1.54) [-0.51 to -1.81]	-1.30 (-0.86 to -1.74) [-0.58 to -2.02]	-1.00±0.34

Table 1: Climate feedback terms and climate sensitivity compared to IPCC Assessment and CMIP models. CMIP6 values taken from Zelinka et al. (2020). ^aInferred values for a linearized system, without strong constraints for the second derivative of planetary emissivity with respect to surface temperature. ^bCombines Planck, WVLR and albedo feedbacks with Ceppi and Nowack (2021) evaluated range for cloud feedback. ^cCombines with Raghuraman et al. (2023) evaluated range for cloud feedback.